

GeoMan: Temporally Consistent Human Geometry Estimation using Image-to-Video Diffusion

Gwanghyun Kim^{1,2*}, Xueting Li¹, Ye Yuan¹, Koki Nagano¹, Tianye Li¹,
Jan Kautz¹, Se Young Chun², Umar Iqbal¹
¹NVIDIA ²Seoul National University

<https://research.nvidia.com/labs/dair/geoman>

Abstract

Estimating accurate and temporally consistent 3D human geometry from videos is a challenging problem in computer vision. Existing methods, primarily optimized for single images, often suffer from temporal inconsistencies and fail to capture fine-grained dynamic details. To address these limitations, we present GeoMan, a novel architecture designed to produce accurate and temporally consistent depth and normal estimations from monocular human videos. GeoMan addresses two key challenges: the scarcity of high-quality 4D training data and the need for metric depth estimation to accurately model human size. To overcome the first challenge, GeoMan employs an image-based model to estimate depth and normals for the first frame of a video, which then conditions a video diffusion model, reframing video geometry estimation task as an image-to-video generation problem. This design offloads the heavy lifting of geometric estimation to the image model and simplifies the video model’s role to focus on intricate details while using priors learned from large-scale video datasets. Consequently, GeoMan improves temporal consistency and generalizability while requiring minimal 4D training data. To address the challenge of accurate human size estimation, we introduce a root-relative depth representation that retains critical human-scale details and is easier to be estimated from monocular inputs, overcoming the limitations of traditional affine-invariant and metric depth representations. GeoMan achieves state-of-the-art performance in both qualitative and quantitative evaluations, demonstrating its effectiveness in overcoming longstanding challenges in 3D human geometry estimation from videos.

1. Introduction

Estimating human 3D geometry [47, 48, 60] from images or videos has enabled numerous applications in digital human and virtual reality. While significant progress [29, 62, 63] has been made, most methods [18, 30, 31] focus on single-

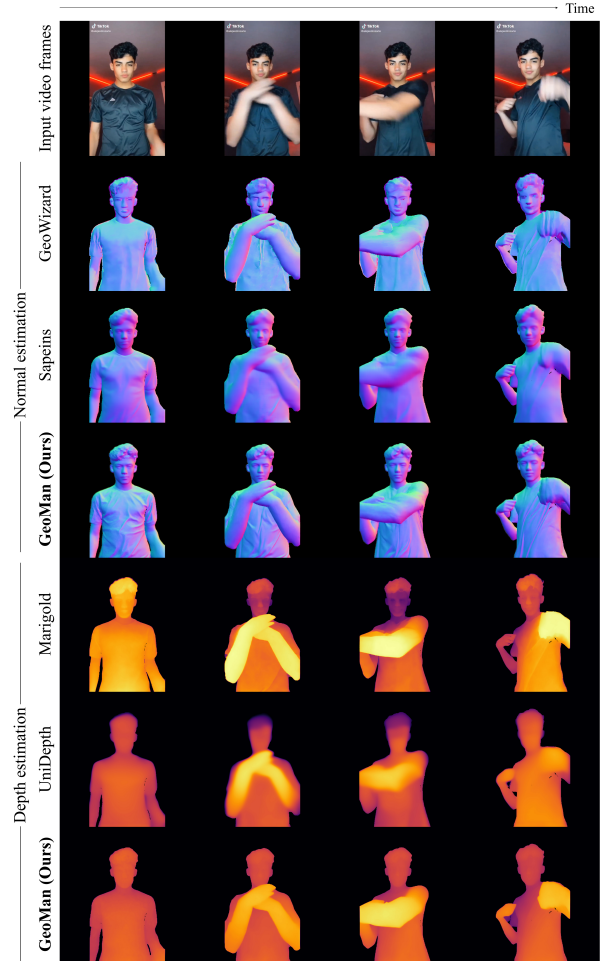


Figure 1. GeoMan provides accurate and temporally stable geometric predictions for human videos, surpassing existing methods.

image geometric estimation. When applied to videos, these methods often struggle with temporal inconsistency, causing visible flickering artifacts and missing fine dynamic details such as subtle facial deformations, clothing wrinkles, and hair movements. These details are crucial for applications involving human motion, as shown in Fig. 1 This work aims to estimate highly accurate and temporally consistent depth and normal from monocular human videos.

*Work done during an internship at NVIDIA.

This is a highly challenging task that presents two difficulties. First, the scarcity of high-quality 4D data poses a significant challenge to training accurate geometry estimation models. Recent works [15, 30] address this limitation by repurposing text-to-image diffusion models for image-based geometry estimation. These methods modify the diffusion denoiser architecture to intake both the input image and geometric information, followed by fine-tuning on image-geometry pairs. Extending these approaches to video geometry estimation introduces additional challenges due to the higher dimensionality and complexity of videos. While some methods [24, 61] have explored adapting video diffusion models to video depth estimation, they often require a substantial amount of high-quality video-depth sequences. For instance, DepthCrafter [24] curates a large-scale dataset including approximately 200K real and synthetic video-depth pairs. Consequently, this strategy cannot be naively extended to human video geometry estimation, as high-quality 4D human data is difficult to collect. The second challenge lies in selecting an appropriate depth representation. Depth estimation from monocular inputs is inherently ambiguous. Most methods resort to predicting affine-invariant depth, which normalizes the depth map using the minimum and maximum depth value for each image or video. While affine-invariant depth simplifies the learning objective and encourages the models to focus on local geometric details, it sacrifices essential size and scale information, particularly for human subjects, resulting in distorted 3D geometry and temporal flickering as presented in Fig. 5. Recent methods [3, 5, 23, 40] have attempted to predict metric depth to address these issues; however, they often do so at the expense of spatial details.

To address these challenges, we introduce *GeoMan*, a novel approach for temporal consistent and accurate depth and normal estimation from monocular human videos. To reduce dependency on 4D training data, we decompose the complex video geometry estimation task into image geometry estimation and image-to-video synthesis. This allows us to maximally exploit the prior in image-to-video diffusion models by introducing minimal changes to the diffusion model architecture. As a result, we maintain its powerful representation capabilities and generalization ability while adapting it for our specific task with limited 4D training data. To achieve this, we first train an image-based model to estimate depth and normal maps of static images. This model is then used to predict geometric information of the first frame of a video, which serves as conditioning input for an image-to-video diffusion model. The video model subsequently infers temporally consistent geometric information for the entire video. Furthermore, GeoMan unifies depth and normal estimation by leveraging a single video diffusion model. This is achieved by simply switching the conditioning image, enabling simultane-

ous training for both modalities (depth and normal) and enhancing generalization across diverse scenarios. Second, to preserve human scale information in depth estimation, GeoMan introduces a root-relative depth representation tailored for human-centric geometry estimation. This representation retains essential metric-scale details while discarding only global translation, facilitating accurate local geometric details estimation. When necessary, absolute translation can be efficiently recovered using state-of-the-art human pose estimation models (e.g., [58, 66]), enabling absolute metric depth estimation. Unlike conventional per-frame or per-video normalization techniques that hinder metric depth recovery and degrade temporal stability by computing independent scale factors per frame or per video, our approach enables consistent and stable depth estimation over time. Our contributions are:

- We propose GeoMan, which repurposes image-to-video diffusion models for temporally consistent depth and normal estimation in human videos, even when trained on limited data.
- We introduce a root-relative depth representation that preserves critical human size information, enabling metric depth estimation and 3D reconstruction.
- Extensive evaluations show that GeoMan surpasses baselines in accuracy and temporal stability, while effectively generalizing to in-the-wild human videos.

2. Related Works

Image-Based Geometry Estimation. Image-based depth and normal estimation has advanced significantly in recent years. By leveraging mixed datasets and powerful diffusion models [4], state-of-the-art approaches such as MiDaS [43], Depth-Anything [62, 63], Marigold [30], and GeoWizard [15] achieve high accuracy and impressive generalization. In parallel, a line of research has focused on human-centric geometry estimation. This approach utilizes either implicit surface regression [1, 17, 47, 48] or parametric body models (e.g., SMPL [39]) [25, 36, 59, 60, 73, 75]. Recently, HDNet [29] proposes a generalizable self-supervision method that leverages large-scale unlabeled human videos for training. Additionally, Sapiens [31] demonstrates strong performance by pretraining on large-scale human image datasets. Despite these advancements, these image-based methods often struggle with temporal consistency and fine geometric details when applied to video geometry estimation, as shown in Fig. 4.

Video Geometry Estimation. To enhance temporal consistency in video geometry estimation, one approach involves test-time optimization [11, 34, 37, 72], which refines predictions using optical flow or camera poses. While effective, this post-processing step is often computationally expensive. Meanwhile, methods [24, 61] developed for generic object video geometry estimation often yield unsatisfying

structs the depth map $\hat{\mathbf{D}}$ from the estimated clean latent $\hat{\mathbf{d}}_0$.

3.2. Controllable Video Generation Models

Using image-to-video (I2V) diffusion models [4, 71], recent video generation methods synthesize videos from a single image by modeling the conditional distribution $p(\mathbf{X}^{(1:F)} | \mathbf{X}^{(1)})$, where $\mathbf{X}^{(1)} \in \mathbb{R}^{3 \times H \times W}$ is an input image and $\mathbf{X}^{(1:F)} \in \mathbb{R}^{F \times 3 \times H \times W}$ represents the generated video frames. Controllable video generation methods [35] incorporate additional guidance (e.g., depth or normal) to enforce structural consistency. This extends the formulation to $p(\mathbf{X}^{(1:F)} | \mathbf{X}^{(1)}, \mathbf{D}^{(1:F)})$, where $\mathbf{D}^{(1:F)} \in \mathbb{R}^{F \times H \times W}$ represents depth or normal maps that provide geometric information. In this work, we formulate video depth and normal estimation as an image-to-video generation task, building our system upon both image geometry estimation models [30] and conditional video generation frameworks [35].

4. GeoMan

GeoMan aims to estimate temporally consistent and accurate depth and normal maps from monocular human videos. Our key idea is to frame video geometry estimation as an image-to-video generation task (Sec. 4.1), leveraging the pre-trained priors of image-to-video models learned with large-scale video datasets. To preserve human scale information in the estimated depth maps, we propose a novel human-centered metric depth representation in Sec. 4.2 that computes root-relative distances as the depth measurement. We explain the process of synthesizing training data to train our models using 3D and 4D human scans in Sec. 4.3.

4.1. Temporal Human Geometry Estimation

Given a monocular RGB video of a single moving human, $\mathbf{X}^{(1:F)} \in \mathbb{R}^{F \times 3 \times H \times W}$, our objective is to estimate dynamic human geometry, including depth maps $\mathbf{D}^{(1:F)} \in \mathbb{R}^{F \times 3 \times H \times W}$ and normal maps $\mathbf{N}^{(1:F)} \in \mathbb{R}^{F \times 3 \times H \times W}$ for all F frames in the video. To reduce dependency on 4D training data, we decompose this complex task into image-geometry estimation and image-to-video synthesis. We begin by training an Image-to-Geometry Estimation Model (I2G) that estimates the depth and normal map of the first frame in a video. This initial estimation serves as guidance for our Video-to-Geometry Estimation Model (V2G), which predicts the depth or normal maps for subsequent frames. As demonstrated in Tab. 5(a) and Fig. 6, our approach reduces reliance on extensive 4D training datasets, while achieving superior performance and strong generalization ability. Fig. 2(a) shows an overview of GeoMan.

Image-to-Geometry Estimation Model (I2G). We predict geometry for the first frame by modeling the conditional distributions $p(\mathbf{D}^{(1)} | \mathbf{X}^{(1)})$ and $p(\mathbf{N}^{(1)} | \mathbf{X}^{(1)})$. Inspired by Marigold [30], we learn a LDM [17] within the

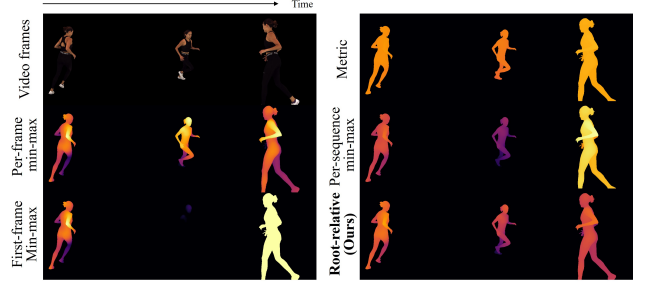


Figure 3. Comparison of depth representations: Our representation offers the highest fidelity and improves temporal modeling.

| Method | Aff-invariant | Metric | Root-relative |
|----------------------|---|---------------|-----------------------|
| Formulation | $\frac{D - \min(D)}{\max(D) - \min(D)}$ | D | $D - d_{\text{root}}$ |
| Range | $[0, 1]$ | $[0, \infty]$ | $[-h/2, h/2]$ |
| Scale preservation | ✗ | ✓ | ✓ |
| Temporal consistency | ✗ | ✓ | ✓ |
| Detail preservation | ✓ | ✗ | ✓ |

Table 1. Comparison of different depth representations. h is the maximum human height. We divide h by 2 because the root keypoint is roughly in the middle of the body.

latent space of a pre-trained VAE model [32] for depth and normal estimation. More details can be found in Sec. 3.1, Sec. B.1 of the supplementary material and in [30]. Note that we learn two separate diffusion models for depth and normal prediction, which yields better performance compared to sharing a single model across two modalities.

Video-to-Geometry Estimation Model (V2G). Given the geometry estimations from the first frame as discussed above, we formulate geometry estimation for the subsequent frames as modeling the conditional distributions $p(\mathbf{D}^{(1:F)} | \mathbf{X}^{(1:F)}, \mathbf{D}^{(1)})$ and $p(\mathbf{N}^{(1:F)} | \mathbf{X}^{(1:F)}, \mathbf{N}^{(1)})$. We adopt a ControlNet-based diffusion model [35] that takes the video frames $\mathbf{X}^{(1:F)}$ as control inputs and the first frame’s geometry (depth $\mathbf{D}^{(1)}$ or normal $\mathbf{N}^{(1)}$) as a reference image. As illustrated in Fig. 2(a), we learn a unified model for both depth and normal estimation, which can be achieved by simply switching the reference image input between depth $\mathbf{D}^{(1)}$ or normal map $\mathbf{N}^{(1)}$ of the first frame. Our intuition is that by framing video geometry estimation as an image-to-video synthesis task, depth and normal maps of the first frame are solely used as a reference image while the fundamental task (i.e., image-to-video synthesis) remains the same for both modalities, hence it enables us to share a single model across two modalities. In the following, we assume the reference image is a normal map, depth estimation can be similarly performed by changing the reference image to a depth map.

At each training step, we map the normal maps to the latent space by a pre-trained encoder and add noise to the normal latents $\mathbf{n}^{(1:F)}$ at a random timestep t . We concatenate the latents of the first frame’s normal with noisy normal latents and pass them to the video denoising model to

estimate the added noise, where the input video frames are injected into the denoising model as control signal using a ControlNet. We adopt the v -objective [49] to ensure stable performance. We optimize the denoiser by minimizing the difference between the estimated and ground truth velocity:

$$\mathcal{L}_{V2G} = \mathbb{E}_{\mathbf{n}_0^{(1:F)}, \epsilon, t} \left\| \mathbf{v}_t - \mathbf{v}_\phi(\mathbf{n}_t^{(1:F)}, \mathbf{n}^{(1)}, \mathbf{X}^{(1:F)}, t) \right\|_2^2, \quad (2)$$

where \mathbf{v}_ϕ denotes our velocity prediction model, $\mathbf{v}_t = \alpha_t \epsilon - \sigma_t \mathbf{n}_0^{(1:F)}$, $\epsilon \sim \mathcal{N}(0, I)$, $t \sim \mathcal{U}(T)$, and $\mathbf{n}_t^{(1:F)}$ represents the noisy normal latents at timestep t . During inference, we start from a sequence of random noise maps and gradually denoise them to normal maps, using the video frames as control signals and the first frame’s normal prediction from I2G as the reference image.

Compared to existing video depth and normal estimation works [29, 31, 60], our V2G model provides two key advantages: 1) *Efficient utilization of pre-trained representations*: By leveraging a pre-trained image-to-video model, we exploit the powerful prior learned from large-scale video datasets. This enables efficient training with less data while enhancing both temporal consistency and geometric accuracy. 2) *Multi-modality compatibility*: The model utilizes shared weights across tasks, toggling between depth and normal estimation by switching the reference image. This enables simultaneous training for both modalities, improving prediction accuracy (See Table 5). As a result, our V2G model demonstrates strong generalizability, effectively handling *long video* sequences and *multi-person* scenarios. Please refer to Sec. C.1 in supplementary for details.

4.2. Human-Centered Root-Relative Depth

A major challenge in monocular depth estimation lies in selecting an optimal depth representation. Most existing methods [30, 31] employ an affine-invariant depth representation with per-frame normalization, which loses crucial information about human scale, and leads to inferior temporal stability. Recent video depth estimation methods [30, 31] introduce per-sequence normalization to improve stability across sequences, though they often struggle to capture fine details effectively. Conversely, methods [3, 5] predicting metric depth directly often sacrifice spatial details, compromising the accuracy of geometry estimation. Fig. 3 provides an intuitive comparison of different depth representations.

To address these limitations, we propose a human-centered root-relative depth representation that preserves metric-scale details while only discarding global translation. This representation ensures accurate human size and scale, which is crucial for tasks requiring precise human geometry (e.g., human reconstruction). As shown in Fig. 2(b), the root-relative depth of each pixel is computed as the distance between the human root (i.e., the pelvis joint) and each point on the human surface. Formally, the root-relative depth $\mathbf{D}^{\text{root-rel}}$ is computed as $\mathbf{D}^{\text{root-rel}} = \mathbf{D}^{\text{metric}} - d^{\text{root}}$,

where $\mathbf{D}^{\text{metric}}$ is the metric depth, d^{root} is the depth of the root joint, which can be obtained via pose estimation techniques [16, 58]. For training, we obtain the root joint’s depth using the SMPL-X [39] annotation in the datasets. Given the SMPL-X pelvis joint location in world space $\mathbf{P}_w \in \mathbb{R}^3$, the camera rotation matrix $\mathbf{R} \in \mathbb{R}^{3 \times 3}$ and translation vector $\mathbf{T} \in \mathbb{R}^3$, we compute the root depth as $d^{\text{root}} = (\mathbf{R}\mathbf{P}_w + \mathbf{T})_z$, as illustrated in Fig. 2(b).

We compare depth representations in Table 1. Root-relative depth offers several key advantages: 1) *Human scale preservation*: It retains the relative depth information of the person in metric scale, allowing inference of real human size. In contrast, affine-invariant depth always normalizes this size to 1, discarding meaningful scale information. Additionally, absolute metric depth can be easily predicted by combining root-relative depth with root depth estimated by advanced human pose prediction models [16, 58]. 2) *Temporal consistency*: Root-relative depth is more temporally stable, as it avoids per-frame normalization using varying $\min(D)$ and $\max(D)$, which is required for affine-invariant depth and can introduce temporal artifacts. 3) *Geometric detail preservation*: The range of root-relative depth is constrained to $[-h/2, h/2]$, determined by the maximum human height (h) and independent of global position. In contrast, metric depth spans a much wider range (e.g., $[0, \infty]$), making it harder for networks to focus on fine-grained geometry, as they must learn large global variations.

4.3. Training with Limited Geometric Video Data

We synthesize our training data by rendering 3D scans from the THuman-2.0 [65] dataset and 4D scans from the XHumans [50, 54] dataset using diverse camera distance, pitch angles, and focal lengths. To train the I2G model, we rendered 40K frames from the THuman-2.0 [65] dataset, which consists of 525 high-resolution, textured 3D scans with approximately 300K vertices per scan. For training the V2G model, we addressed the limited diversity in sequences and subjects by combining data from the XHumans [50] dataset (233 sequences across 20 subjects) with augmented data derived from THuman-2.0. To leverage the static 3D scans in THuman-2.0, we transform multiview images into simulated videos that mimic camera rotation.

In total, our model is trained using only 20 subjects in 4D [50] and around 500 subjects in 3D [65] from public datasets. This dataset is significantly smaller compared to the large-scale proprietary datasets employed by state-of-the-art methods [29, 31]. Despite limited data, our approach demonstrates strong performance, underscoring its efficiency and robustness.

5. Experiments

We present comprehensive videos at [our project page](#) to visually evaluate dynamic geometry estimation. The

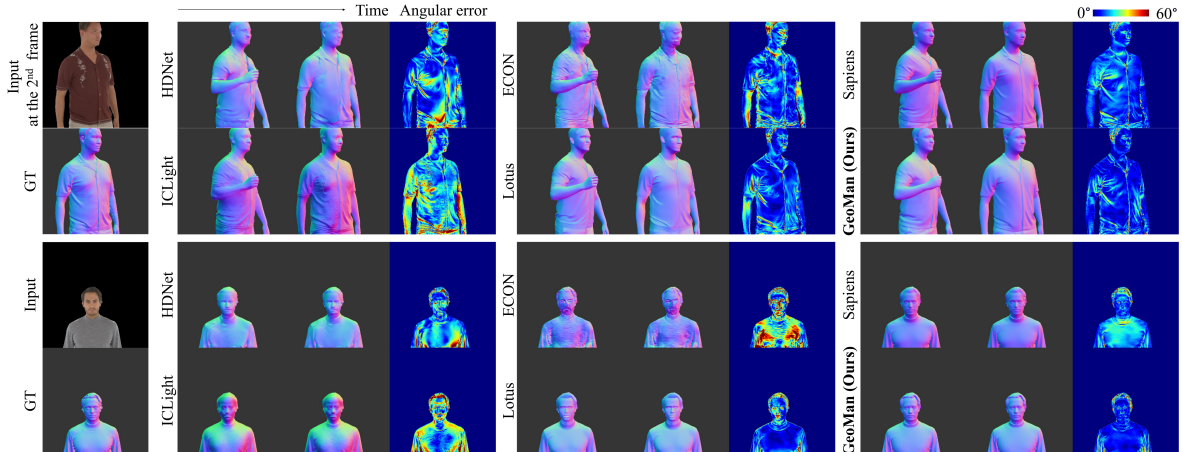


Figure 4. Zero-shot normal estimation comparison on ActorsHQ. **Left**: Predicted normal for the first frame. **Middle**: Predicted normal for the second frame. **Right**: Angular error visualization for the second frame.

| | Performance on moving subject videos | | | | Performance on moving camera videos | | | | Temporal consistency | | |
|----------------------|--------------------------------------|---------------|---------------|---------------|-------------------------------------|---------------|---------------|---------------|----------------------|--------------|---------------|
| | Mean↓ | Median↓ | 11.25°↑ | 30°↑ | Mean↓ | Median↓ | 11.25°↑ | 30°↑ | OPW↓ | TC-Mean↓ | TC-11.25°↑ |
| ECON [60] | 29.228 | 23.766 | 17.963 | 62.464 | 27.202 | 22.089 | 19.652 | 66.682 | 0.173 | 16.371 | 50.469 |
| ICLight [69] | 27.996 | 23.555 | 16.384 | 64.276 | 26.975 | 22.529 | 17.595 | 66.567 | 0.122 | 11.476 | 66.866 |
| HDNet [29] | 24.477 | 20.329 | 21.737 | 71.527 | 23.954 | 19.867 | 22.493 | 72.764 | 0.134 | 12.398 | 62.957 |
| GeoWizard [15] | 22.714 | 19.151 | 23.446 | 75.610 | 22.054 | 18.520 | 24.796 | 76.981 | 0.178 | 16.584 | 43.846 |
| Lotus [18] | 18.780 | 14.937 | 34.947 | 83.743 | 18.101 | 14.444 | 36.605 | 85.217 | 0.079 | 8.782 | 79.397 |
| Sapiens* [31] | 18.338 | 14.526 | 36.498 | 85.009 | 18.048 | 14.425 | 36.706 | 85.760 | 0.094 | 9.494 | 77.567 |
| Sapiens [31] | 16.278 | 13.015 | 41.245 | 89.177 | 16.099 | 12.941 | 41.539 | 89.617 | 0.082 | 7.861 | 82.803 |
| GeoMan (Ours) | 16.185 | 12.334 | 45.217 | 87.784 | 15.535 | 11.657 | 48.168 | 88.789 | 0.070 | 6.876 | 96.757 |

Table 2. Comparison on zero-shot normal estimation on ActorsHQ dataset. Sapiens*: fine-tuned on our dataset. GeoMan outperforms state-of-the-art methods despite using only public data, unlike Sapiens which was trained using large-scale proprietary data. The drop in performance of Sapiens when fine-tuned on our dataset highlights the importance of its proprietary data in its performance.

supplementary material also includes implementation details, evaluation specifics, additional results on the Goliath dataset [38], in-the-wild videos, long videos, and multi-person scenarios.

Evaluation Dataset. We use ActorsHQ [27] as our primary evaluation dataset for its high-quality dynamic geometry ($\sim 30K$ vertices) and independence from training sets. For evaluation, we generate 192 videos of moving subjects with static cameras and 256 videos with moving cameras and static subjects. The full evaluation dataset includes more than 10K frames rendered at 512×512 resolution. Additional results on the Tiktok [28] and the Goliath [38] dataset can be found in Sec. C.2 and Sec. C.3 of the supplementary.

5.1. Surface Normal Estimation

Baselines. We compare our method against baselines including HDNet [28, 29], ECON [60], and Sapiens [31], which are state-of-the-art normal estimation models trained on human-centric data. Notably, methods like Sapiens and HDNet were trained using proprietary human-centric datasets, whereas our model was trained on publicly available datasets. Additionally, we compare against models trained for generic scenes, such as GeoWizard [15], Lotus [18], and ICLight [69]. For all comparisons, we used the

official checkpoints provided by the authors. Additionally, we report the performance of Sapiens, the best-performing baseline, fine-tuned on our dataset.

Metrics. We report mean and median angular error, along with the percentage of pixels within t° error for $t \in \{11.25^\circ, 30^\circ\}$. To assess temporal consistency, we provide the optical flow-based warping metric (OPW) [7], as well as the optical flow-based angular error (TC-Mean) and the 11.25° metric (TC-11.25°).

Results. As shown in Table 2, GeoMan outperforms previous approaches, achieving higher accuracy in normal prediction and better temporal consistency. While GeoMan significantly outperforms other methods, Sapiens [31] performs competitively. However, it is important to note that Sapiens was trained on a proprietary dataset. For a fair comparison, we also fine-tune Sapiens’s pre-trained MAE model on our dataset. As we can see, under this more fair setting, GeoMan outperforms Sapiens by a notable margin. Fig. 4 presents a qualitative comparison, demonstrating that GeoMan delivers more consistent estimations over time and higher fidelity.



Figure 5. Comparison with existing depth estimation models. GeoMan achieves state-of-the-art performance in both depth prediction (top row in each result) and point cloud reconstruction (bottom row), excelling in temporal consistency, fidelity, and scale preservation.

| | Performance on moving subject videos | | | | Performance on moving camera videos | | | | Temporal consistency | | |
|--------------------------------------|--------------------------------------|--------------|--------------------------|-------------------|-------------------------------------|--------------|--------------------------|-------------------|----------------------|--------------|-----------------|
| | Absolute | | Optimizing scale + shift | | Absolute | | Optimizing scale + shift | | OPW↓ | TC-RMSE↓ | TC- δ 1↑ |
| | δ 1↑ | SI-log10↓ | AbsRel↓ | $\delta < 1.05$ ↑ | δ 1↑ | SI-log10↓ | AbsRel↓ | $\delta < 1.05$ ↑ | | | |
| ZoeDepth [3] | 0.016 | 2.710 | 0.016 | 0.960 | 0.000 | 2.487 | 0.018 | 0.955 | 0.058 | 0.017 | 0.830 |
| UniDepth [40] | 0.058 | 8.027 | 0.025 | 0.883 | 0.003 | 7.790 | 0.022 | 0.915 | 0.128 | 0.031 | 0.564 |
| Depth pro [5] | 0.127 | 5.297 | 0.026 | 0.865 | 0.103 | 5.804 | 0.025 | 0.882 | 0.201 | 0.046 | 0.388 |
| Metric3Dv2 [23] | 0.491 | 6.213 | 0.016 | 0.958 | 0.697 | 5.804 | 0.019 | 0.944 | 0.085 | 0.023 | 0.743 |
| GeoMan (Ours) | 0.972 | 2.116 | 0.011 | 0.984 | 0.987 | 1.775 | 0.009 | 0.992 | 0.038 | 0.015 | 0.898 |
| GeoMan w GT root-depth (Ours) | 0.998 | 2.118 | 0.011 | 0.984 | 0.998 | 1.775 | 0.009 | 0.992 | 0.032 | 0.015 | 0.915 |

Table 3. Comparison with metric depth estimation methods on zero-shot settings on ActorsHQ dataset.

| | Performance on moving subject videos | | | | Performance on moving camera videos | | | | Temporal consistency | | |
|----------------------|--------------------------------------|-------------------|--------------------------|-------------------|-------------------------------------|-------------------|--------------------------|-------------------|----------------------|--------------|-----------------|
| | Optimizing shift | | Optimizing scale + shift | | Optimizing shift | | Optimizing scale + shift | | OPW↓ | TC-RMSE↓ | TC- δ 1↑ |
| | AbsRel↓ | $\delta < 1.05$ ↑ | AbsRel↓ | $\delta < 1.05$ ↑ | AbsRel↓ | $\delta < 1.05$ ↑ | AbsRel↓ | $\delta < 1.05$ ↑ | | | |
| HDNet [29] | 0.031 | 0.808 | 0.024 | 0.877 | 0.030 | 0.821 | 0.021 | 0.921 | 0.108 | 0.027 | 0.604 |
| Sapiens [31] | 0.040 | 0.680 | 0.009 | 0.986 | 0.041 | 0.663 | 0.010 | 0.987 | 0.058 | 0.018 | 0.792 |
| Sapiens* [31] | 0.021 | 0.915 | 0.015 | 0.959 | 0.017 | 0.960 | 0.013 | 0.980 | 0.054 | 0.018 | 0.816 |
| Marigold [30] | 0.021 | 0.901 | 0.021 | 0.901 | 0.015 | 0.956 | 0.017 | 0.951 | 0.074 | 0.027 | 0.547 |
| GeoWizard [15] | 0.018 | 0.935 | 0.019 | 0.930 | 0.014 | 0.967 | 0.017 | 0.952 | 0.053 | 0.023 | 0.667 |
| Lotus [18] | 0.022 | 0.899 | 0.019 | 0.919 | 0.016 | 0.954 | 0.015 | 0.962 | 0.077 | 0.025 | 0.637 |
| DepthCrafter [24] | 0.016 | 0.944 | 0.013 | 0.967 | 0.012 | 0.976 | 0.018 | 0.945 | 0.037 | 0.016 | 0.914 |
| Depth-Any-Video [61] | 0.018 | 0.928 | 0.015 | 0.955 | 0.014 | 0.971 | 0.018 | 0.948 | 0.039 | 0.017 | 0.823 |
| GeoMan (Ours) | 0.012 | 0.978 | 0.011 | 0.984 | 0.009 | 0.991 | 0.009 | 0.992 | 0.032 | 0.014 | 0.915 |

Table 4. Comparison with affine-invariant depth estimation methods in zero-shot on ActorsHQ. Sapiens*: fine-tuned on our dataset.

5.2. Depth Estimation

Baselines. For metric depth estimation, we compare with state-of-the-art methods including Metric3Dv2 [23], UniDepth [40], ZoeDepth [3], and Depth Pro [5]. For affine-invariant depth estimation, we benchmark against

image-based models such as Sapiens [31], Marigold [30], GeoWizard [15], and Lotus [18]. Additionally, we include video-based methods like DepthCrafter [24] and Depth Any Video [61], which are trained on large-scale video datasets. For all baselines, we used official checkpoints.

| | Normal | | | | | | Depth | | | | | |
|--|--------------------|---------|------------|----------------------|----------|------------------|----------|--------------------------|----------|----------------------|----------|--|
| | Angular difference | | %within t° | Temporal consistency | | Optimizing shift | | Optimizing scale + shift | | Temporal consistency | | |
| | Mean↓ | Median↓ | 11.25°↑ | OPW↓ | TC-Mean↓ | AbsRel↓ | δ <1.05↑ | AbsRel↓ | δ <1.05↑ | OPW↓ | TC-RMSE↓ | |
| (a) Naive extension vs GeoMan across training steps | | | | | | | | | | | | |
| Naïve-5K-steps | 25.305 | 22.732 | 15.602 | 0.076 | 7.458 | 0.038 | 0.720 | 0.028 | 0.856 | 0.049 | 0.019 | |
| Naïve-30K steps | 19.669 | 16.628 | 28.405 | 0.072 | 7.169 | 0.020 | 0.926 | 0.017 | 0.943 | 0.040 | 0.016 | |
| GeoMan-5K steps | 17.499 | 13.541 | 40.340 | 0.069 | 6.781 | 0.014 | 0.964 | 0.013 | 0.970 | 0.036 | 0.014 | |
| GeoMan-30K steps | 16.185 | 12.334 | 45.217 | 0.070 | 6.876 | 0.012 | 0.978 | 0.011 | 0.984 | 0.032 | 0.014 | |
| (b) Naive extension vs GeoMan on 1/10 training data (at 30K steps) | | | | | | | | | | | | |
| Naïve w/ 1/10 data | 22.329 | 19.626 | 20.568 | 0.068 | 6.833 | NaN | NaN | NaN | NaN | NaN | NaN | |
| GeoMan w/ 1/10 data | 17.679 | 13.559 | 40.263 | 0.065 | 6.451 | 0.013 | 0.975 | 0.011 | 0.982 | 0.032 | 0.014 | |
| (c) Multimodality of V2G | | | | | | | | | | | | |
| Unimodal | 16.260 | 12.361 | 45.091 | 0.073 | 7.190 | 0.012 | 0.976 | 0.011 | 0.983 | 0.038 | 0.015 | |
| Multimodal | 16.185 | 12.334 | 45.217 | 0.070 | 6.876 | 0.012 | 0.978 | 0.011 | 0.984 | 0.032 | 0.014 | |
| (d) Source of the first frame for V2G | | | | | | | | | | | | |
| GT+V2G | 14.028 | 10.101 | 54.924 | 0.078 | 7.536 | 0.009 | 0.985 | 0.009 | 0.988 | 0.032 | 0.014 | |
| I2G+V2G | 16.185 | 12.334 | 45.217 | 0.070 | 6.876 | 0.012 | 0.978 | 0.011 | 0.984 | 0.032 | 0.014 | |

Table 5. Ablation studies. We validate the impact of various design choices.

Metrics. For metric depth estimation, we follow existing methods [5] and report δ_1 and SI-log10 (Scale-Invariant Logarithmic Error). The root depth is obtained using 3D pose estimation method [58] to convert our predictions to metric depth. For evaluating affine-invariant depth estimation methods, we align the predicted depth maps with the ground truth using two approaches: (1) optimizing only the shift to highlight the benefits of GeoMan’s learned human scale, and (2) optimizing both scale and shift before computing the metrics. We report AbsRel (absolute relative error) and $\delta < 1.05$ (the percentage of pixels where $\max(d/\hat{d}, \hat{d}/d) < 1.05$). We further report affine-invariant metrics for metric depth estimation methods to provide a comprehensive assessment. To evaluate temporal consistency, we report the optical flow-based warping metric (OPW) [57], RMSE, and the δ_1 metric. Details of all metrics can be found in Sec. B.3 in the supplementary.

Results. Table 3 summarizes the results for metric depth estimation. GeoMan significantly outperforms other methods, demonstrating its effectiveness. Notably, we outperform the second-best method Metric3Dv2 by 100% and 65% in terms of δ_1 and SI-log10, respectively. ZoeDepth performs best in terms of temporal consistency but yields significantly worse accuracy metrics, due to overly smooth predictions (See Fig. 5). Additionally, instead of using the pose estimation method VIMO [58] to estimate the root joint depth, we also evaluate performance using ground-truth root depth. This further improves the results, highlighting the potential for additional enhancements in future works. Table 4 compares GeoMan with affine-invariant depth estimation methods. When optimizing only the shift, our model achieves the best results, showcasing the advantages of our proposed root-relative depth representation in capturing human-scale information. Our method outperforms most baselines with both scale and shift optimization while maintaining superior temporal consistency.

Fig. 5 presents a qualitative comparison with baselines. All depth maps are renormalized using sequence-wise min-

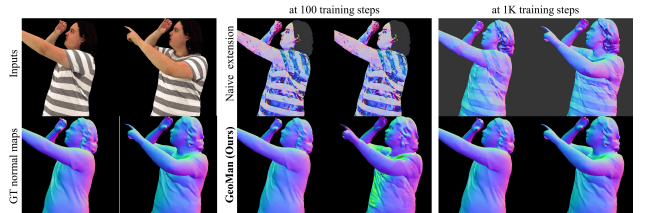


Figure 6. Comparison of naïve extension and GeoMan across training steps. Results here are evaluated on the validation data.

max scaling within the human mask to ensure consistency, following [31]. Compared to per-frame estimation models, our approach produces more temporally stable results. While UniDepth [40] and DepthCrafter [24] improve temporal consistency, our model achieves higher accuracy both visually and quantitatively. The second row of Fig. 5 compares point cloud reconstructions (PCD) generated by our method and baselines, where pixels are lifted into 3D space using the predicted depth and camera parameters provided in the dataset. Prior methods produce distorted and temporally inconsistent reconstructions, whereas GeoMan ensures accurate scaling and superior temporal consistency.

5.3. Ablation Studies and Analysis

Naïve Extension vs. GeoMan. We compare our approach with a naïve extension of [24, 30]. In this extension, instead of decomposing the task into I2G and V2G as in GeoMan, a video diffusion model is trained to predict normal or depth maps for all frames in a single pass without employing a control module. This design suffers from the task gap and fails to effectively utilize prior knowledge, resulting in sub-optimal performance. Evaluation results at different training iterations are presented in Table 5(a). Notably, GeoMan achieves superior performance even at early ($\sim 5K$) iterations, outperforming the naïve extension approach at 30K iterations. This performance gap arises because directly predicting geometric information for all frames deviates significantly from the original task of the video diffusion model. As a result, naïve extension fails to effectively leverage its prior, as can be seen in Fig. 6. We further demonstrate Geo-

Man’s superior generalization ability by training both models on a reduced dataset (1/10 of the original), the naïve extension approach suffers significantly, with poor performance in the normal model and NaN scores in the depth model as presented in Table 5(b). This highlights the effectiveness of our I2G and V2G model in utilizing pre-trained priors for its representation and generalization capacity.

Multimodality of V2G. Another advantage of GeoMan’s image-to-video formulation is its ability to share model weights between the normal and depth prediction by simply switching the reference image. This enables training on multi-modal data, improving both generalization and training efficiency. Table 5(c) shows that the multi-modal model achieves superior results compared to task specific models, demonstrating the effectiveness of our formulation.

Source of the First Frame for V2G. Tab. 5(d) shows that replacing I2G predictions with ground-truth normal or depth improves V2G’s performance, highlighting the potential for further gains by refining the image-based I2G model.

6. Conclusion

We introduce GeoMan, a novel framework for accurate and temporally consistent depth and normal estimation from monocular videos. GeoMan addresses the challenge of 4D human data scarcity by framing the video geometry estimation task as image-to-video synthesis. To preserve human scale information, we proposed a root-relative depth representation tailored for human geometry. Extensive experiments on high-resolution benchmarks showed that GeoMan surpasses existing methods, even those trained on large-scale proprietary data, demonstrating effectiveness in real-world video geometry estimation and 3D reconstruction.

References

- [1] Thiemo Alldieck, Mihai Zanfir, and Cristian Sminchisescu. Photorealistic monocular 3d reconstruction of humans wearing clothing. *CVPR*, 2022. 2
- [2] Omer Bar-Tal, Hila Chefer, Omer Tov, Charles Herrmann, Roni Paiss, Shiran Zada, Ariel Ephrat, Junhwa Hur, Yuanzhen Li, Tomer Michaeli, et al. Lumiere: A space-time diffusion model for video generation. *arXiv preprint arXiv:2401.12945*, 2024. 3
- [3] Shariq Farooq Bhat, Reiner Birkel, Diana Wofk, Peter Wonka, and Matthias Müller. Zoedepth: Zero-shot transfer by combining relative and metric depth. *arXiv preprint arXiv:2302.12288*, 2023. 2, 3, 5, 7
- [4] Andreas Blattmann, Tim Dockhorn, Sumith Kulal, Daniel Mendelevitch, Maciej Kilian, Dominik Lorenz, Yam Levi, Zion English, Vikram Voleti, Adam Letts, et al. Stable video diffusion: Scaling latent video diffusion models to large datasets. *arXiv:2311.15127*, 2023. 2, 3, 4
- [5] Aleksei Bochkovskii, Amaël Delaunoy, Hugo Germain, Marcel Santos, Yichao Zhou, Stephan R. Richter, and Vladlen Koltun. Depth pro: Sharp monocular metric depth in less than a second. *arXiv:2410.02073*, 2024. 2, 3, 5, 7, 8
- [6] Tim Brooks, Bill Peebles, Connor Holmes, Will DePue, Yufei Guo, Li Jing, David Schnurr, Joe Taylor, Troy Luhman, Eric Luhman, Clarence Ng, Ricky Wang, and Aditya Ramesh. Video generation models as world simulators, 2024. 3
- [7] Thomas Brox, Andrés Bruhn, Nils Papenberg, and Joachim Weickert. High accuracy optical flow estimation based on a theory for warping. *ECCV*, 2004. 6
- [8] Wenhao Chai, Xun Guo, Gaoang Wang, and Yan Lu. Stable-video: Text-driven consistency-aware diffusion video editing. In *Proceedings of the IEEE/CVF International Conference on Computer Vision*, pages 23040–23050, 2023. 3
- [9] Haoxin Chen, Menghan Xia, Yingqing He, Yong Zhang, Xiaodong Cun, Shaoshu Yang, Jinbo Xing, Yaofang Liu, Qifeng Chen, Xintao Wang, et al. Videocrafter1: Open diffusion models for high-quality video generation. *arXiv preprint arXiv:2310.19512*, 2023.
- [10] Haoxin Chen, Yong Zhang, Xiaodong Cun, Menghan Xia, Xintao Wang, Chao Weng, and Ying Shan. Videocrafter2: Overcoming data limitations for high-quality video diffusion models. *CVPR*, 2024. 3
- [11] Yuhua Chen, Cordelia Schmid, and Cristian Sminchisescu. Self-supervised learning with geometric constraints in monocular video: Connecting flow, depth, and camera. *ICCV*, 2019. 2
- [12] Ming Ding, Wendi Zheng, Wenyi Hong, and Jie Tang. Cogview2: Faster and better text-to-image generation via hierarchical transformers. *NeurIPS*, 2022. 3
- [13] David Eigen, Christian Puhrsch, and Rob Fergus. Depth map prediction from a single image using a multi-scale deep network. *NeurIPS*, 2014. 12
- [14] Patrick Esser, Johnathan Chiu, Parmida Atighehchian, Jonathan Granskog, and Anastasis Germanidis. Structure and content-guided video synthesis with diffusion models. *ICCV*, 2023. 3
- [15] Xiao Fu, Wei Yin, Mu Hu, Kaixuan Wang, Yuexin Ma, Ping Tan, Shaojie Shen, Dahua Lin, and Xiaoxiao Long. GeoWizard: Unleashing the diffusion priors for 3d geometry estimation from a single image. *ECCV*, 2024. 2, 3, 6, 7
- [16] Shubham Goel, Georgios Pavlakos, Jathushan Rajasegaran, Angjoo Kanazawa, and Jitendra Malik. Humans in 4D: Reconstructing and tracking humans with transformers. *ICCV*, 2023. 5
- [17] Sang-Hun Han, Min-Gyu Park, Ju Hong Yoon, Ju-Mi Kang, Young-Jae Park, and Hae-Gon Jeon. High-fidelity 3d human digitization from single 2k resolution images. *CVPR*, 2023. 2, 4
- [18] Jing He, Haodong Li, Wei Yin, Yixun Liang, Leheng Li, Kaiqiang Zhou, Hongbo Liu, Bingbing Liu, and Ying-Cong Chen. Lotus: Diffusion-based visual foundation model for high-quality dense prediction. *arXiv preprint arXiv:2409.18124*, 2024. 1, 3, 6, 7
- [19] Yingqing He, Tianyu Yang, Yong Zhang, Ying Shan, and Qifeng Chen. Latent video diffusion models for high-fidelity video generation with arbitrary lengths. In *arXiv preprint arXiv:2211.13221*, 2022. 3
- [20] Jonathan Ho, Ajay Jain, and Pieter Abbeel. Denoising diffusion probabilistic models. *NeurIPS*, 2020. 3

- [21] Jonathan Ho, Tim Salimans, Alexey Gritsenko, William Chan, Mohammad Norouzi, and David J Fleet. Video diffusion models. *arXiv:2204.03458*, 2022. 3
- [22] Li Hu, Xin Gao, Peng Zhang, Ke Sun, Bang Zhang, and Liefeng Bo. Animate anyone: Consistent and controllable image-to-video synthesis for character animation. In *arXiv*, 2023. 3
- [23] Mu Hu, Wei Yin, Chi Zhang, Zhipeng Cai, Xiaoxiao Long, Hao Chen, Kaixuan Wang, Gang Yu, Chunhua Shen, and Shaojie Shen. Metric3d v2: A versatile monocular geometric foundation model for zero-shot metric depth and surface normal estimation. *arXiv preprint arXiv:2404.15506*, 2024. 2, 7
- [24] Wenbo Hu, Xiangjun Gao, Xiaoyu Li, Sijie Zhao, Xiaodong Cun, Yong Zhang, Long Quan, and Ying Shan. DepthCrafter: Generating consistent long depth sequences for open-world videos. *arXiv preprint arXiv:2409.02095*, 2024. 2, 3, 7, 8, 12, 14, 18
- [25] Zeng Huang, Yuanlu Xu, Christoph Lassner, Hao Li, and Tony Tung. ARCH: Animatable reconstruction of clothed humans. *CVPR*, 2020. 2
- [26] Zhaoyang Huang, Xiaoyu Shi, Chao Zhang, Qiang Wang, Ka Chun Cheung, Hongwei Qin, Jifeng Dai, and Hongsheng Li. Flowformer: A transformer architecture for optical flow. In *European conference on computer vision*, pages 668–685. Springer, 2022. 13
- [27] Mustafa İşik, Martin Rünz, Markos Georgopoulos, Taras Khakhulin, Jonathan Starck, Lourdes Agapito, and Matthias Nießner. HumanRF: High-fidelity neural radiance fields for humans in motion. *ACM Transactions on Graphics (TOG)*, 42(4):1–12, 2023. 6
- [28] Y. Jafarian and H. Park. Self-supervised 3d representation learning of dressed humans from social media videos. *TPAMI*, 2022. 6
- [29] Yasamin Jafarian and Hyun Soo Park. Learning high fidelity depths of dressed humans by watching social media dance videos. *CVPR*, 2021. 1, 2, 5, 6, 7
- [30] Bingxin Ke, Anton Obukhov, Shengyu Huang, Nando Metzger, Rodrigo Caye Daudt, and Konrad Schindler. Repurposing diffusion-based image generators for monocular depth estimation. *CVPR*, 2024. 1, 2, 3, 4, 5, 7, 8, 18
- [31] Rawal Khirrodar, Timur Bagautdinov, Julieta Martinez, Su Zhaoen, Austin James, Peter Selednik, Stuart Anderson, and Shunsuke Saito. Sapiens: Foundation for human vision models. *ECCV*, 2024. 1, 2, 5, 6, 7, 8, 15
- [32] DP Kingma. Auto-encoding variational bayes. *arXiv preprint arXiv:1312.6114*, 2013. 3, 4
- [33] Diederik P Kingma. Adam: A method for stochastic optimization. *arXiv preprint arXiv:1412.6980*, 2014. 12
- [34] Johannes Kopf, Xuejian Rong, and Jia-Bin Huang. Robust consistent video depth estimation. *CVPR*, 2021. 2
- [35] Han Lin, Jaemin Cho, Abhay Zala, and Mohit Bansal. Ctrl-Adapter: An efficient and versatile framework for adapting diverse controls to any diffusion model. *arXiv preprint arXiv:2404.09967*, 2024. 3, 4, 12
- [36] Matthew Loper, Naureen Mahmood, Javier Romero, Gerard Pons-Moll, and Michael J. Black. SMPL: A skinned multi-person linear model. *SIGGRAPH Asia*, 2015. 2
- [37] Xuan Luo, Jia-Bin Huang, Richard Szeliski, Kevin Matzen, and Johannes Kopf. Consistent video depth estimation. *ACM Transactions on Graphics (TOG)*, 39(4), 2020. 2
- [38] Julieta Martinez, Emily Kim, Javier Romero, Timur Bagautdinov, Shunsuke Saito, Shou-I Yu, Stuart Anderson, Michael Zollhöfer, Te-Li Wang, Shaojie Bai, Chenghui Li, Shih-En Wei, Rohan Joshi, Wyatt Borsos, Tomas Simon, Jason Saragih, Paul Theodosis, Alexander Greene, Anjani Josyula, Silvio Mano Maeta, Andrew I. Jewett, Simon Venstain, Christopher Heilman, Yueh-Tung Chen, Sidi Fu, Mohamed Ezzeldin A. Elshaer, Tingfang Du, Longhua Wu, Shen-Chi Chen, Kai Kang, Michael Wu, Youssef Emad, Steven Longay, Ashley Brewer, Hitesh Shah, James Booth, Taylor Koska, Kayla Haidle, Matt Andromalos, Joanna Hsu, Thomas Daur, Peter Selednik, Tim Godisart, Scott Ardisson, Matthew Cipperly, Ben Humberston, Lon Farr, Bob Hansen, Peihong Guo, Dave Braun, Steven Krenn, He Wen, Lucas Evans, Natalia Fadeeva, Matthew Stewart, Gabriel Schwartz, Divam Gupta, Gyeongsik Moon, Kaiwen Guo, Yuan Dong, Yichen Xu, Takaaki Shiratori, Fabian Prada, Bernardo R. Pires, Bo Peng, Julia Buffalini, Autumn Trimble, Kevyn McPhail, Melissa Schoeller, and Yaser Sheikh. Codec Avatar Studio: Paired Human Captures for Complete, Driveable, and Generalizable Avatars. *NeurIPS*, 2024. 6, 12, 15
- [39] Georgios Pavlakos, Vasileios Choutas, Nima Ghorbani, Timo Bolkart, Ahmed A. A. Osman, Dimitrios Tzionas, and Michael J. Black. Expressive body capture: 3D hands, face, and body from a single image. *CVPR*, 2019. 2, 5
- [40] Luigi Piccinelli, Yung-Hsu Yang, Christos Sakaridis, Mattia Segu, Siyuan Li, Luc Van Gool, and Fisher Yu. UniDepth: Universal monocular metric depth estimation. *CVPR*, 2024. 2, 3, 7, 8
- [41] Dustin Podell, Zion English, Kyle Lacey, Andreas Blattmann, Tim Dockhorn, Jonas Müller, Joe Penna, and Robin Rombach. SDXL: Improving latent diffusion models for high-resolution image synthesis. *ICLR*, 2023. 3
- [42] Aditya Ramesh, Prafulla Dhariwal, Alex Nichol, Casey Chu, and Mark Chen. Hierarchical text-conditional image generation with clip latents. *arXiv preprint arXiv:2204.06125*, 2022. 3
- [43] René Ranftl, Katrin Lasinger, David Hafner, Konrad Schindler, and Vladlen Koltun. Towards robust monocular depth estimation: Mixing datasets for zero-shot cross-dataset transfer. *TPAMI*, 44(3):1623–1637, 2020. 2
- [44] Robin Rombach, Andreas Blattmann, Dominik Lorenz, Patrick Esser, and Björn Ommer. High-resolution image synthesis with latent diffusion models. *CVPR*, 2022. 3
- [45] Nataniel Ruiz, Yuanzhen Li, Varun Jampani, Yael Pritch, Michael Rubinstein, and Kfir Aberman. Dreambooth: Fine tuning text-to-image diffusion models for subject-driven generation. *CVPR*, 2023. 3
- [46] Chitwan Saharia, William Chan, Saurabh Saxena, Lala Li, Jay Whang, Emily L Denton, Kamyar Ghasemipour, Raphael Gontijo Lopes, Burcu Karagol Ayan, Tim Salimans, et al. Photorealistic text-to-image diffusion models with deep language understanding. *NeurIPS*, 2022. 3

- [47] Shunsuke Saito, Zeng Huang, Ryota Natsume, Shigeo Morishima, Angjoo Kanazawa, and Hao Li. Pifu: Pixel-aligned implicit function for high-resolution clothed human digitization. *CVPR*, 2019. 1, 2
- [48] Shunsuke Saito, Tomas Simon, Jason Saragih, and Hanbyul Joo. Pifuhd: Multi-level pixel-aligned implicit function for high-resolution 3d human digitization. *CVPR*, 2020. 1, 2
- [49] Tim Salimans and Jonathan Ho. Progressive distillation for fast sampling of diffusion models. *ICLR*, 2022. 3, 5
- [50] Kaiyue Shen, Chen Guo, Manuel Kaufmann, Juan Zarate, Julien Valentin, Jie Song, and Otmar Hilliges. X-Avatar: Expressive human avatars. *CVPR*, 2023. 5
- [51] Jascha Sohl-Dickstein, Eric Weiss, Niru Maheswaranathan, and Surya Ganguli. Deep unsupervised learning using nonequilibrium thermodynamics. *ICML*, 2015. 3
- [52] Patrick von Platen, Suraj Patil, Anton Lozhkov, Pedro Cuenca, Nathan Lambert, Kashif Rasul, Mishig Davaadorj, Dhruv Nair, Sayak Paul, William Berman, Yiyi Xu, Steven Liu, and Thomas Wolf. Diffusers: State-of-the-art diffusion models. <https://github.com/huggingface/diffusers>, 2022. 12
- [53] Jiuniu Wang, Hangjie Yuan, Dayou Chen, Yingya Zhang, Xiang Wang, and Shiwei Zhang. Modelscape text-to-video technical report. In *arXiv*, 2023. 3
- [54] Wenbo Wang, Hsuan-I Ho, Chen Guo, Boxiang Rong, Artur Grigorev, Jie Song, Juan Jose Zarate, and Otmar Hilliges. 4D-DRESS: A 4d dataset of real-world human clothing with semantic annotations. *CVPR*, 2024. 5
- [55] Weimin Wang, Jiawei Liu, Zhijie Lin, Jiangqiao Yan, Shuo Chen, Chetwin Low, Tuyen Hoang, Jie Wu, Jun Hao Liew, Hanshu Yan, et al. MagicVideo-V2: Multi-stage high-aesthetic video generation. *arXiv preprint arXiv:2401.04468*, 2024. 3
- [56] Xiang Wang, Hangjie Yuan, Shiwei Zhang, Dayou Chen, Jiuniu Wang, Yingya Zhang, Yujun Shen, Deli Zhao, and Jingren Zhou. Videocomposer: Compositional video synthesis with motion controllability. *NeurIPS*, 2023. 3
- [57] Yiran Wang, Zhiyu Pan, Xingyi Li, Zhiguo Cao, Ke Xian, and Jianming Zhang. Less is more: Consistent video depth estimation with masked frames modeling. In *ACM MM*, 2022. 8, 13
- [58] Yufu Wang, Ziyun Wang, Lingjie Liu, and Kostas Daniilidis. TRAM: Global trajectory and motion of 3d humans from in-the-wild videos. In *Proc. European Conf. on Computer Vision (ECCV)*, pages 467–487, 2024. 2, 5, 8, 12
- [59] Yuliang Xiu, Jinlong Yang, Dimitrios Tzionas, and Michael J Black. ICON: Implicit clothed humans obtained from normals. *CVPR*, 2022. 2
- [60] Yuliang Xiu, Jinlong Yang, Xu Cao, Dimitrios Tzionas, and Michael J. Black. ECON: Explicit Clothed humans Optimized via Normal integration. *CVPR*, 2023. 1, 2, 5, 6
- [61] Honghui Yang, Di Huang, Wei Yin, Chunhua Shen, Haifeng Liu, Xiaofei He, Binbin Lin, Wanli Ouyang, and Tong He. Depth any video with scalable synthetic data. *arXiv preprint arXiv:2410.10815*, 2024. 2, 3, 7
- [62] Lihe Yang, Bingyi Kang, Zilong Huang, Xiaogang Xu, Jiashi Feng, and Hengshuang Zhao. Depth anything: Unleashing the power of large-scale unlabeled data. *CVPR*, 2024. 1, 2
- [63] Lihe Yang, Bingyi Kang, Zilong Huang, Zhen Zhao, Xiaogang Xu, Jiashi Feng, and Hengshuang Zhao. Depth anything v2. *arXiv:2406.09414*, 2024. 1, 2
- [64] Wei Yin, Chi Zhang, Hao Chen, Zhipeng Cai, Gang Yu, Kaixuan Wang, Xiaozhi Chen, and Chunhua Shen. Metric3d: Towards zero-shot metric 3d prediction from a single image. *ICCV*, 2023. 3
- [65] Tao Yu, Zerong Zheng, Kaiwen Guo, Pengpeng Liu, Qionghai Dai, and Yebin Liu. Function4d: Real-time human volumetric capture from very sparse consumer rgbd sensors. *CVPR*, 2021. 5
- [66] Ye Yuan, Umar Iqbal, Pavlo Molchanov, Kris Kitani, and Jan Kautz. GLAMR: Global occlusion-aware human mesh recovery with dynamic cameras. *CVPR*, 2022. 2
- [67] Lvmin Zhang, Anyi Rao, and Maneesh Agrawala. Adding conditional control to text-to-image diffusion models. In *Proceedings of the IEEE/CVF International Conference on Computer Vision*, pages 3836–3847, 2023. 3
- [68] Lvmin Zhang, Anyi Rao, and Maneesh Agrawala. Adding conditional control to text-to-image diffusion models. *ICCV*, 2023. 3
- [69] Lvmin Zhang, Anyi Rao, and Maneesh Agrawala. IC-light github page, 2024. 6
- [70] Shiwei Zhang, Jiayu Wang, Yingya Zhang, Kang Zhao, Hangjie Yuan, Zhiwu Qin, Xiang Wang, Deli Zhao, and Jingren Zhou. I2vgen-xl: High-quality image-to-video synthesis via cascaded diffusion models. *arXiv preprint arXiv:2311.04145*, 2023. 12
- [71] Shiwei* Zhang, Jiayu* Wang, Yingya* Zhang, Kang Zhao, Hangjie Yuan, Zhiwu Qing, Xiang Wang, Deli Zhao, and Jingren Zhou. I2VGen-XL: High-quality image-to-video synthesis via cascaded diffusion models. In *arXiv:2311.04145*, 2023. 3, 4
- [72] Zhoutong Zhang, Forrester Cole, Richard Tucker, William T Freeman, and Tali Dekel. Consistent depth of moving objects in video. *ACM Transactions on Graphics (TOG)*, 40(4):1–12, 2021. 2
- [73] Zechuan Zhang, Zongxin Yang, and Yi Yang. SIFU: Side-view conditioned implicit function for real-world usable clothed human reconstruction. *CVPR*, 2024. 2
- [74] Peng Zheng, Dehong Gao, Deng-Ping Fan, Li Liu, Jorma Laaksonen, Wanli Ouyang, and Nicu Sebe. Bilateral reference for high-resolution dichotomous image segmentation. *CAAI Artificial Intelligence Research*, 3:9150038, 2024. 12
- [75] Zerong Zheng, Tao Yu, Yebin Liu, and Qionghai Dai. PaMIR: Parametric model-conditioned implicit representation for image-based human reconstruction. *TPAMI*, 2021. 2
- [76] Daquan Zhou, Weimin Wang, Hanshu Yan, Weiwei Lv, Yizhe Zhu, and Jiashi Feng. Magicvideo: Efficient video generation with latent diffusion models. *arXiv preprint arXiv:2211.11018*, 2022. 3
- [77] Shenhao Zhu, Junming Leo Chen, ZuoZhuo Dai, Yinghui Xu, Xun Cao, Yao Yao, Hao Zhu, and Siyu Zhu. Champ: Controllable and consistent human image animation with 3d parametric guidance. *ECCV*, 2024. 14

Supplementary Material of

GeoMan: Temporally Consistent Human Geometry Estimation using Image-to-Video Diffusion

In this documents, we provide additional results and details. We highly encourage readers to view our supplementary video introduced in [our project page](#). We include more experimental and evaluation details in Sec. A. Additional results, including geometry estimation on long videos and multi-person videos, quantitative evaluation on the Goliath dataset [38] and more ablation studies are present in Sec. B. Finally, we discuss the limitations of GeoMan and future works in Sec. C.

A. Experimental Details

A.1. Implementation Details

We implemented the Image Geometry Diffusion (I2G) model based on the pretrained weights of Stable Diffusion 2 and the Video Geometry Diffusion (V2G) model using the pretrained weights of I2VGen-XL [70], initializing Video ControlNet with CtrlAdapter [35], and leveraging the `diffusers` library [52].

As shown in Fig. 2 of the main paper, the VAE encoder-decoder and Video ControlNet remain frozen, while only the diffusion denoiser, V2G, is fine-tuned.

Note that we learn separate diffusion models for image-based normal and depth map estimation. This is because predicting depth and normal from RGB images requires a diffusion model to map an RGB image to two significantly different outputs, thus separate models outperform a single model.

Both models are trained at 512×512 resolution using the Adam optimizer [33] with a learning rate of $1e-5$. I2G is trained for 20K iterations with a batch size of 144, taking approximately two days on 4 NVIDIA A100 GPUs. V2G is trained on 12-frame sequences for 30K iterations with a batch size of 8, requiring approximately three days on 8 A100 GPUs. Evaluation is performed on 32-frame inputs for moving subject videos and 16-frame inputs for moving camera videos. For all experiments, we set the number of denoising steps to 100 and use an ensemble size of 8.

We preprocess input images by removing backgrounds, cropping the human region, and resizing images to a resolution of 512×512 . For inference on in-the-wild videos, we employ video matting method, BiRefNet [74], to remove backgrounds. This preprocessing ensures that our model focuses solely on human-centric geometry while maintaining robustness across diverse scenarios.

A.2. Evaluation Details

Evaluation Dataset The original ActorsHQ dataset includes eight actors performing 15 sequences, captured with 160 cameras at 25 fps. For the evaluation, we generate 192 videos of moving subjects with static cameras (eight actors, 24 cameras, 32 frames per video) at various body scales. we also construct 256 videos with moving cameras and static subjects (32 cameras, 16 frames per video).

Depth Alignment For 'Optimizing shift' in the comparison of depth estimation methods, we optimized the shift per frame with the ground truth depth maps. For 'Optimizing scale + shift,' we optimized the scale per sequence following [24] and optimized the shift per frame.

Point Cloud Reconstruction Root depth is estimated using a 3D pose estimation method [58] to convert predictions into metric depth. Point cloud reconstruction is performed using the dataset's camera intrinsic parameters. While we present unaligned reconstructions, we also align depth predictions to ground truth using an optimized shift to highlight scale differences, as shown in Figs. S11–S14.

Fine-tuning Sapiens on Our Training Dataset For the fine-tuning of Sapiens*, we use the pretrained Sapiens-2B model, which serves as the foundation model trained on a large-scale human dataset. We fine-tune this model specifically for the normal and root-relative depth estimation using our training dataset, following their fine-tuning pipeline ¹.

A.3. Metrics

For evaluating the predicted depth, we follow [13] and use the following metrics:

¹<https://github.com/facebookresearch/sapiens>

$$\begin{aligned}
\text{Abs Relative: } & \frac{1}{\sum(K_t=1)} \sum_{k_t \in K, d_t \in D_t} k_t \left\| \frac{d_t - d_t^{gt}}{d_t^{gt}} \right\| \\
\text{Squared Relative: } & \frac{1}{\sum(K_t=1)} \sum_{k_t \in K, d_t \in D_t} \frac{\|d_t - d_t^{gt}\|^2}{d_t^{gt}} \\
\text{RMSE (linear): } & \sqrt{\frac{1}{\sum(K_t=1)} \sum_{k_t \in K, d_t \in D_t} \|d_t - d_t^{gt}\|^2} \\
\text{RMSE (log): } & \sqrt{\frac{1}{\sum(K_t=1)} \sum_{k_t \in K, d_t \in D_t} \|\log d_t - \log d_t^{gt}\|^2} \\
\delta < \text{thr: } & \frac{1}{\sum(K_t=1)} \sum_{k_t \in K, d_t \in D_t} K_t \left[\text{Max} \left(\frac{D_t}{D_t^{gt}}, \frac{D_t^{gt}}{D_t} \right) < \text{thr} \right] \\
\delta 1: & \frac{1}{\sum(K_t=1)} \sum_{k_t \in K, d_t \in D_t} K_t \left[\text{Max} \left(\frac{D_t}{D_t^{gt}}, \frac{D_t^{gt}}{D_t} \right) < 1.25 \right] \\
\text{SI-log10: } & \sqrt{\frac{1}{\sum(K_t=1)} \sum_{k_t \in K, d_t \in D_t} \|\log_{10}(d_t) - \log_{10}(d_t^{gt})\|^2}
\end{aligned} \tag{S3}$$

where K_t is a depth validity mask, D_t is the predicted depth for image I_t , and D_t^{gt} is the ground-truth depth.

For evaluating the predicted normal maps, we use the metrics from Sapiens. The angular error is computed as the mean and median angular errors between predicted normal vectors and ground-truth normal vectors:

$$\text{Angular Error} = \frac{1}{n} \sum_{i=1}^n \cos^{-1} \left(\frac{\mathbf{n}_i \cdot \mathbf{n}_i^{gt}}{|\mathbf{n}_i| |\mathbf{n}_i^{gt}|} \right) \tag{S4}$$

Additionally, we compute the percentage of pixels where the angular error is below specific thresholds:

$$\text{Percentage of Pixels with Angular Error} < t^\circ = \frac{1}{n} \sum_{i=1}^n \mathbb{I} \left(\cos^{-1} \left(\frac{\mathbf{n}_i \cdot \mathbf{n}_i^{gt}}{|\mathbf{n}_i| |\mathbf{n}_i^{gt}|} \right) < t \right) \tag{S5}$$

where $t \in \{11.5^\circ, 20^\circ\}$.

For evaluating temporal consistency, we introduce optical flow-based metrics. The optical flow-based warping metric (OPW) is defined by [57] as:

$$OPW = \frac{1}{n} \sum_{i=1}^n \sum_{t=0}^{T-1} W_{t+1 \Rightarrow t}^{(i)} \|D_{t+1}^{(i)} - \hat{D}_t^{(i)}\|_1, \tag{S6}$$

where $W_{t+1 \Rightarrow t}^{(i)}$ is the optical flow-based visibility mask calculated from the warping discrepancy between subsequent frames, as explained in [57]. We use the optical flow generated by the latest SOTA FlowFormer [26]. This metric is applied to both depth and normal frames, where the depth and normal values are warped between consecutive frames.

To further encourage comprehensive evaluation of temporal consistency, we introduce additional metrics. For normal frames, we use the following:

$$\text{TC-Mean (Optical Flow-based Angular Error)} = \frac{1}{n} \sum_{i=1}^n \frac{1}{T-1} \sum_{t=0}^{T-1} W_{t+1 \Rightarrow t}^{(i)} \cos^{-1} \left(\frac{\hat{\mathbf{n}}_t^{(i)} \cdot \mathbf{n}_{t+1}^{(i)}}{|\hat{\mathbf{n}}_t^{(i)}| |\mathbf{n}_{t+1}^{(i)}|} \right) \tag{S7}$$

$$\text{TC-11.25}^\circ \text{ (Optical Flow-based Angular Error)} = \frac{1}{n} \sum_{i=1}^n \frac{1}{T-1} \sum_{t=0}^{T-1} W_{t+1 \Rightarrow t}^{(i)} \mathbb{I} \left(\cos^{-1} \left(\frac{\hat{\mathbf{n}}_t^{(i)} \cdot \mathbf{n}_{t+1}^{(i)}}{|\hat{\mathbf{n}}_t^{(i)}| |\mathbf{n}_{t+1}^{(i)}|} \right) < 11.25^\circ \right) \tag{S8}$$

where $\hat{\mathbf{n}}_t^{(i)}$ is the warped normal for the i -th sample at frame t , and $\mathbf{n}_{t+1}^{(i)}$ is the depth from the next frame.

For depth frames, we define the following temporal consistency metric:

$$\text{TC-RMSE (Optical Flow-based Temporal Consistency)} = \sqrt{\frac{1}{n} \sum_{i=1}^n \frac{1}{T-1} \sum_{t=0}^{T-1} W_{t+1 \Rightarrow t}^{(i)} \|\hat{D}_t^{(i)} - D_{t+1}^{(i)}\|^2} \tag{S9}$$

$$\text{TC-}\delta_1 \text{ (Optical Flow-based Depth Consistency)} = \frac{1}{n} \sum_{i=1}^n \frac{1}{T-1} \sum_{t=0}^{T-1} W_{t+1 \Rightarrow t}^{(i)} \mathbb{I} \left(\max \left(\frac{\hat{D}_t^{(i)}}{D_{t+1}^{(i)}}, \frac{D_{t+1}^{(i)}}{\hat{D}_t^{(i)}} \right) < 1.25 \right) \tag{S10}$$

where $\hat{D}_t^{(i)}$ is the warped depth for the i -th sample at frame t , and $D_{t+1}^{(i)}$ is the depth from the next frame.

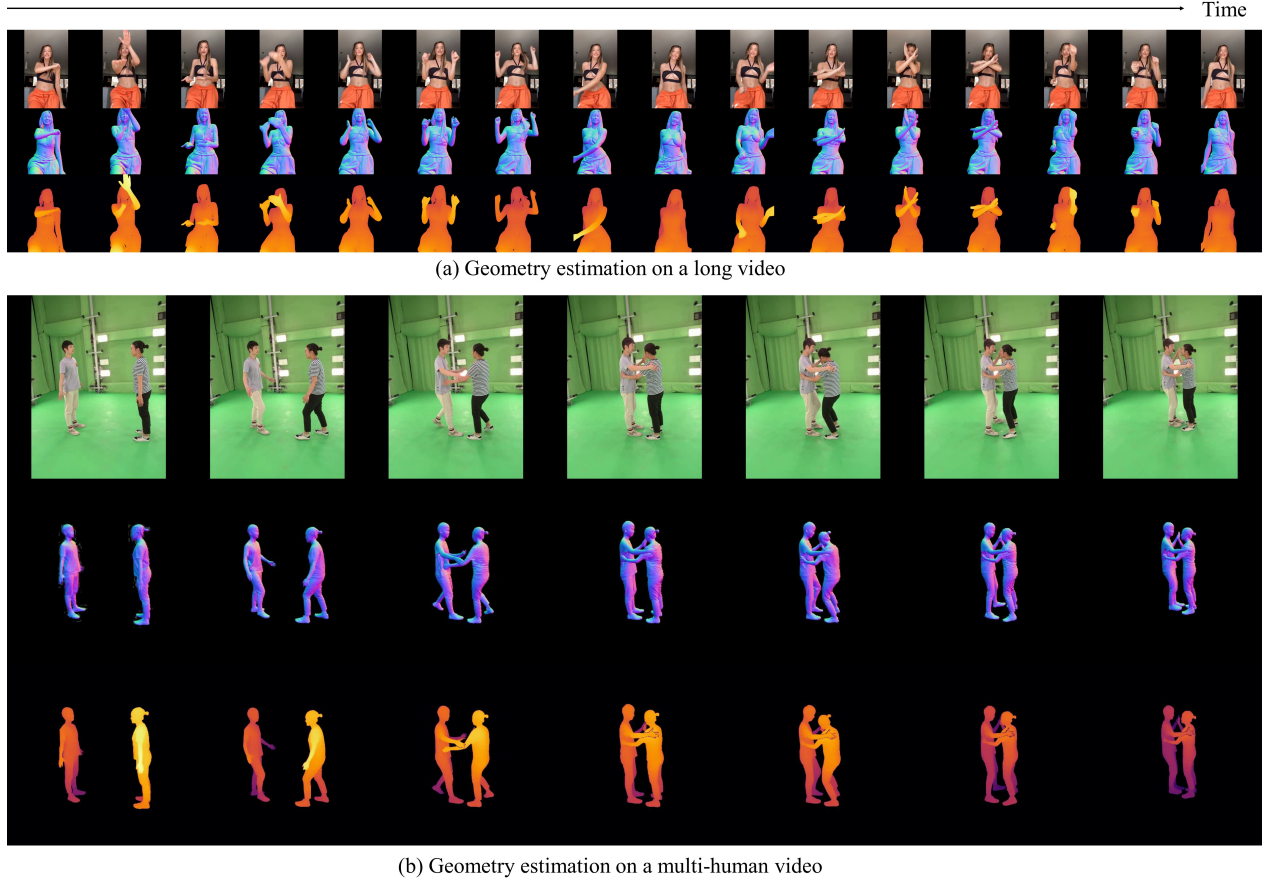


Figure S7. Results of geometry estimation on long and multi-person videos.

B. Additional Qualitative and Quantitative Results

B.1. Geometry Estimation on Long Videos and Multi-Person Videos

Our model effectively generalizes to long video sequences and multi-person scenarios (Fig. S7). Despite being trained on fixed-length sequences, it supports inference on 64-frame sequences using an NVIDIA A100, leveraging robust temporal modeling and extending further via autoregressive inference.

To ensure smooth transitions across segments, we adopt the mortise-and-tenon-style latent interpolation from [24]. Overlapping frames between segments are interpolated with linearly decreasing weights, and the final depth and normal sequences are reconstructed by decoding the stitched latent representations via the VAE decoder.

For multi-person scenarios, our approach remains effective despite training on single-person data. Normal estimation requires no modification, as pretrained priors enable natural adaptation. For depth estimation, we address root-relative ambiguity via per-subject masking and result aggregation. Human masks segment individuals, root-relative depths are estimated, and metric depths are reconstructed via 3D pose estimation, ensuring globally consistent depth while preserving per-subject geometric integrity.

B.2. Qualitative Results on In-the-Wild Videos

To evaluate generalization to in-the-wild videos, we perform a qualitative comparison on short-form videos collected in Champ [77], which compiles content from platforms such as Bilibili, Kuaishou, TikTok, YouTube, and Xiaohongshu. This dataset includes a diverse range of individuals in full-body, half-body, and close-up shots, with varying ages, ethnicities, genders, and backdrops.

As shown in Fig. S8 and S9, our results demonstrate robust performance and high-quality geometry in these in-the-wild videos.

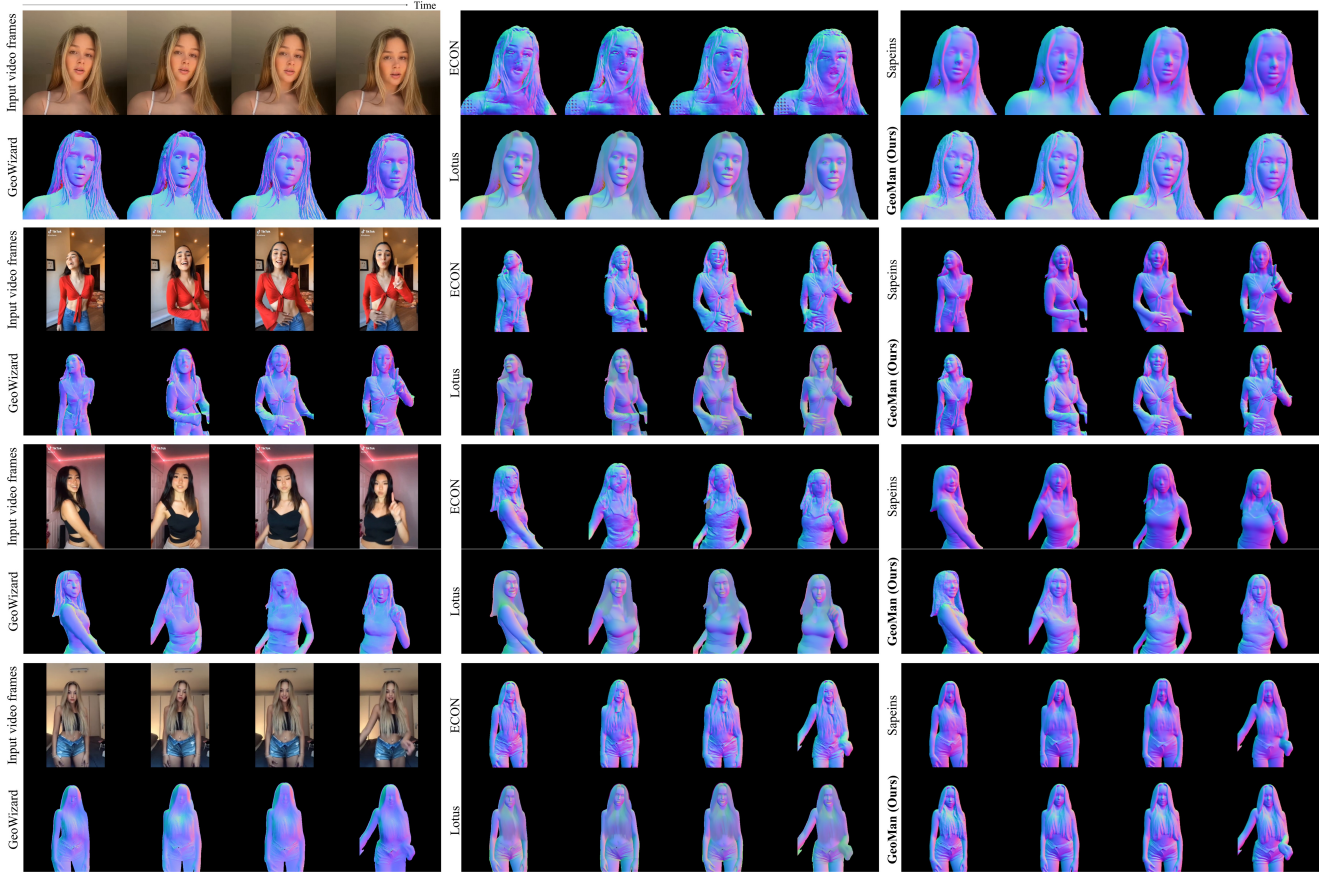


Figure S8. Comparison on zero-shot normal estimation results on in-the-wild videos.

B.3. Quantitative Results on Goliath Dataset

| | Performance on moving subject videos | | | | | | Temporal consistency | | |
|----------------------|--------------------------------------|-------------------------|--------------------|--------------------------|-------------------------|--------------------|----------------------|--------------|------------------------|
| | Optimizing shift | | | Optimizing scale + shift | | | | | |
| | AbsRel↓ | $\delta < 1.05\uparrow$ | $\delta 1\uparrow$ | AbsRel↓ | $\delta < 1.05\uparrow$ | $\delta 1\uparrow$ | OPW↓ | TC-RMSE↓ | TC- $\delta 1\uparrow$ |
| Sapiens | 0.030 | 0.807 | 1.000 | 0.007 | 0.994 | 1.000 | 0.077 | 0.024 | 0.754 |
| Sapiens* | 0.017 | 0.954 | 1.000 | 0.011 | 0.986 | 1.000 | 0.064 | 0.022 | 0.855 |
| Marigold | 0.022 | 0.900 | 1.000 | 0.020 | 0.904 | 1.000 | 0.098 | 0.031 | 0.605 |
| GeoWizard | 0.018 | 0.933 | 1.000 | 0.015 | 0.955 | 0.999 | 0.061 | 0.024 | 0.709 |
| Lotus | 0.023 | 0.888 | 1.000 | 0.022 | 0.898 | 1.000 | 0.097 | 0.031 | 0.680 |
| Depthcrafter | 0.015 | 0.957 | 1.000 | 0.011 | 0.985 | 1.000 | 0.039 | 0.019 | 0.919 |
| Depth any video | <u>0.015</u> | 0.960 | 1.000 | 0.013 | 0.979 | 0.999 | <u>0.044</u> | <u>0.020</u> | 0.866 |
| GeoMan (Ours) | 0.011 | 0.987 | 1.000 | <u>0.010</u> | <u>0.989</u> | 1.000 | 0.038 | 0.018 | <u>0.909</u> |

Table S6. Comparison with affine-invariant depth estimation methods on zero-shot settings on Goliath. Sapiens*: Finetuned on our dataset.

We provide additional quantitative results on the Goliath [38] dataset, a multiview video dataset designed for studying complete avatars, including full-body geometry and underlying body shape. Each instance consists of eight captures of the same person, with four sequences featuring four subjects in full-body capture. For our evaluation, we used 10 views with 32 frames as the test set.

As shown in Table S7 and S6, while GeoMan significantly outperforms other methods, the pre-trained version of Sapiens [31] remains competitive. However, it is important to note that Sapiens was trained on a proprietary dataset. To ensure a fair comparison, we fine-tuned Sapiens’s pre-trained MAE model on our dataset. Under this fair setting, GeoMan outperforms Sapiens by a notable margin.

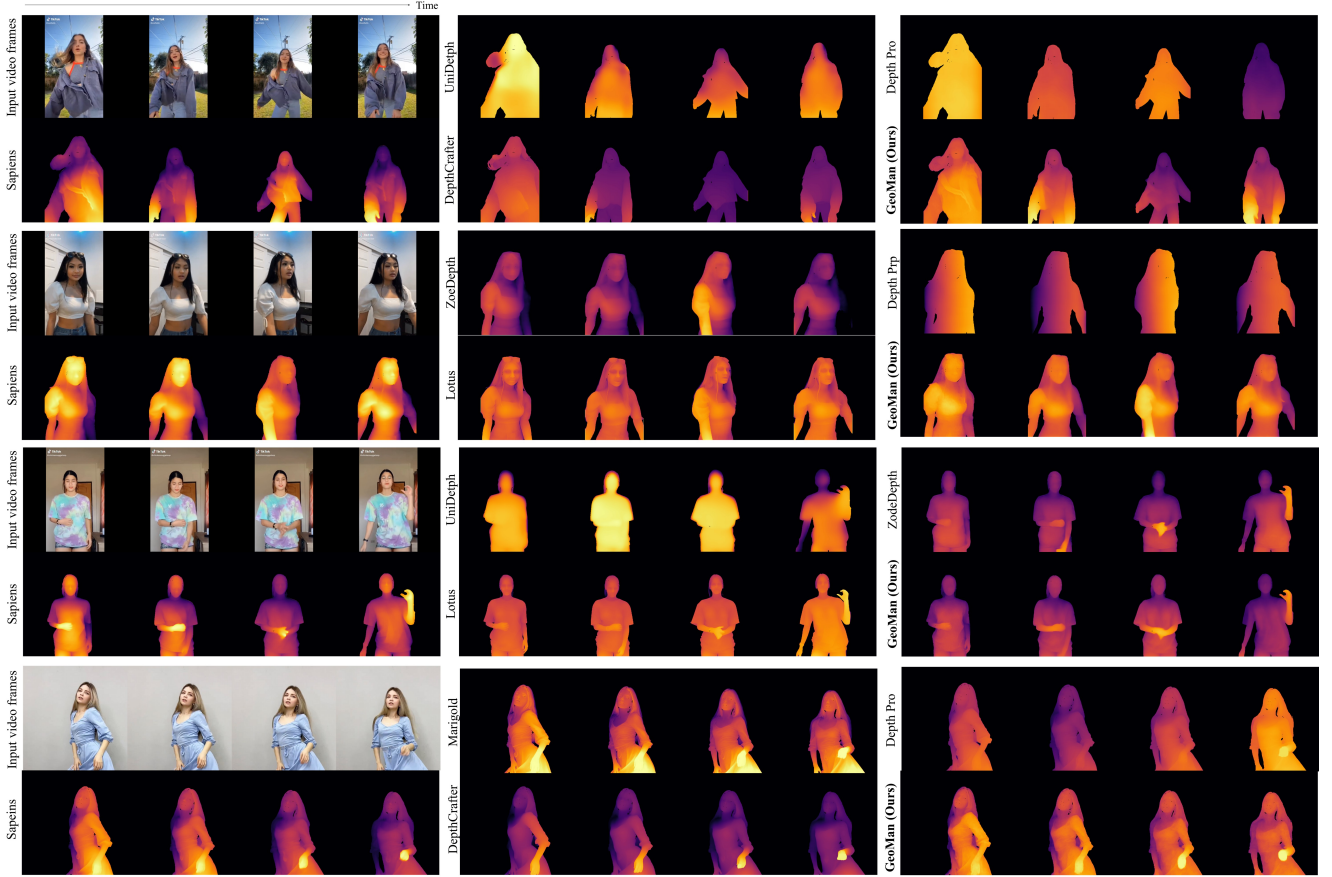


Figure S9. Comparison on zero-shot depth estimation results on in-the-wild videos.

| | Performance on moving subject videos | | | | Temporal consistency | | |
|---------------|--------------------------------------|---------------|---------------|---------------|----------------------|--------------|---------------|
| | Mean↓ | Median↓ | 11.25°↑ | 30°↑ | OPW↓ | TC-Mean↓ | TC-11.25°↑ |
| ECON | 25.498 | 20.129 | 21.800 | 72.345 | 0.196 | 16.280 | 53.385 |
| Sapiens | 11.205 | 8.856 | 64.284 | 96.091 | 0.104 | 9.653 | 77.615 |
| Sapiens* | 13.531 | 10.605 | 53.533 | 93.712 | 0.113 | 10.812 | 74.594 |
| GeoWizard | 19.622 | 16.167 | 30.789 | 82.829 | 0.190 | 18.037 | 41.474 |
| Lotus | 17.999 | 14.766 | 35.198 | 86.666 | 0.104 | 10.155 | 75.924 |
| ICLight | 27.664 | 24.571 | 14.084 | 63.199 | 0.169 | 14.513 | 56.882 |
| GeoMan (Ours) | <u>12.831</u> | <u>10.034</u> | <u>56.665</u> | <u>94.308</u> | 0.084 | 8.128 | 82.811 |

Table S7. Comparison on zero-shot normal estimation on Goliath. Sapiens*: Fine-tuned on our dataset.

B.4. Additional Results on ActorsHQ

Fig. S10 presents additional qualitative comparisons in surface normal estimation, demonstrating that our method not only achieves superior accuracy over baselines but also ensures greater temporal consistency and higher fidelity.

Figs. S11–S16 provide further qualitative comparisons with baseline methods for both moving camera and moving subject videos. To ensure consistency, all predicted depth maps are renormalized using sequence-wise min-max scaling within the human mask. Compared to per-frame estimation models, our approach produces more temporally stable results.

For point cloud reconstruction, we present both unaligned reconstructions and those with depth aligned to ground truth using an optimized shift to emphasize scale differences. Our method effectively preserves human scale, demonstrating strong geometric consistency.

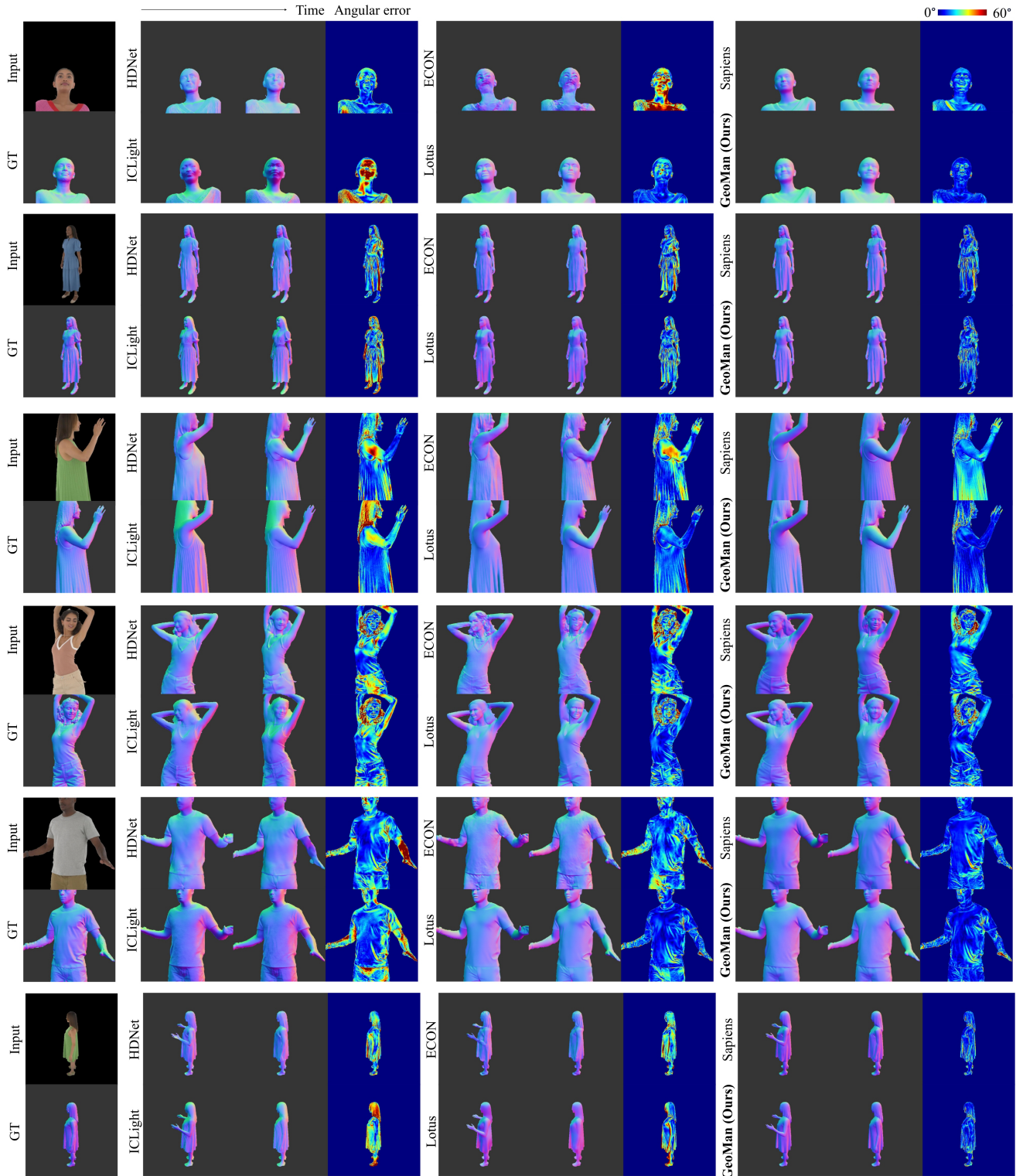


Figure S10. Comparison on zero-shot normal estimation on ActorsHQ. **Left**: Predicted normal. **Right**: Visualization of angular error.



Figure S11. Comparison with the existing depth estimation models. GeoMan produces the state-of-the-art results in both temporal consistency and fidelity.

B.5. Additional Ablation Studies and Analysis

Naïve extension vs. GeoMan Fine-Tuning. In our experiments, we rigorously compare the performance of our proposed image-to-video formulation of GeoMan against a naïve extension of [24, 30]. Despite training for further 50K steps, the naïve extension strategy consistently yields suboptimal results across multiple metrics. As highlighted in Tab. S8(a), the

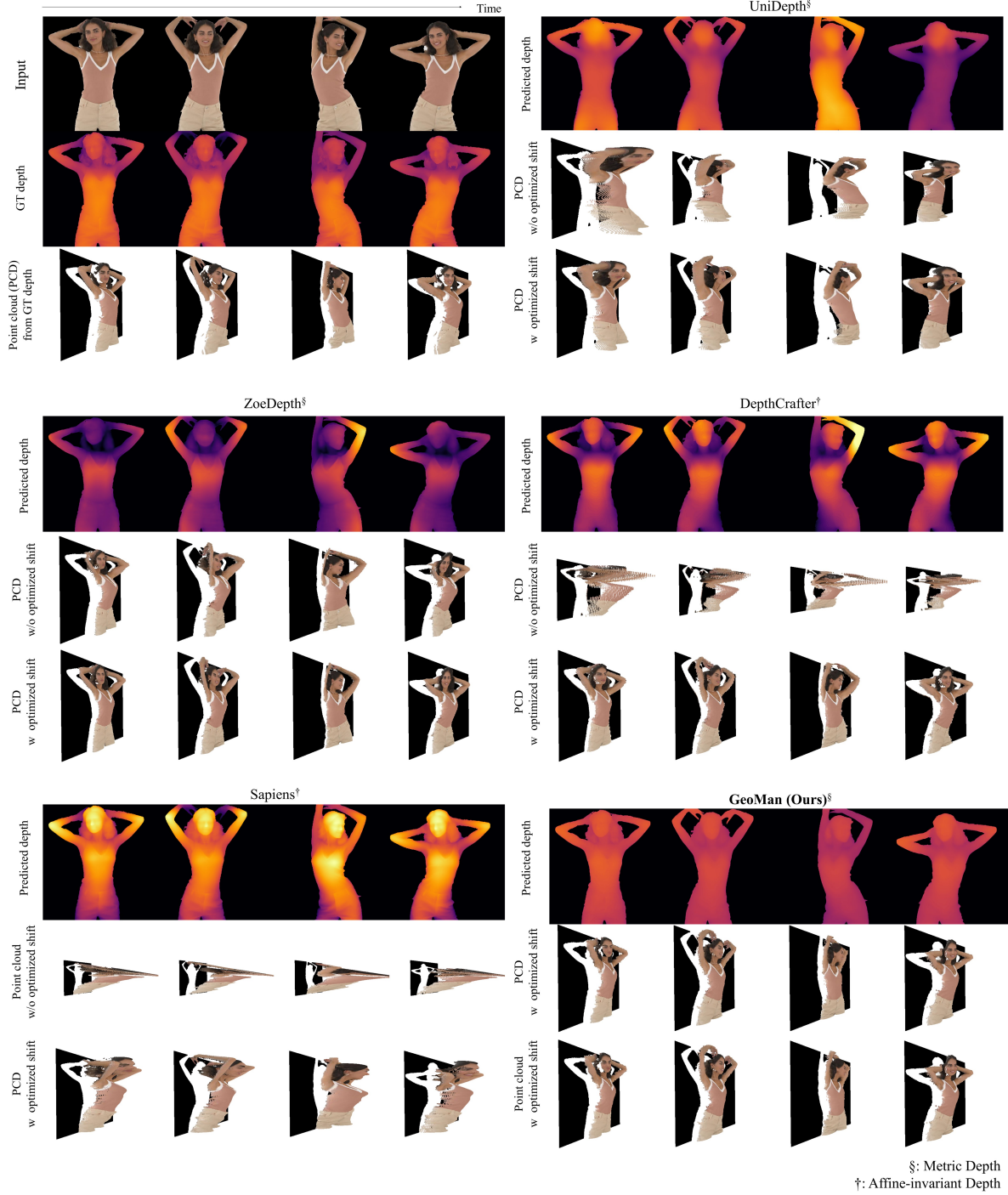


Figure S12. Comparison with the existing depth estimation models. GeoMan produces the state-of-the-art results in both temporal consistency and fidelity.

performance gap remains significant, reinforcing the superior efficiency and effectiveness of our GeoMan approach in handling complex video generation tasks. This stark contrast in performance emphasizes the importance of a more structured, model-specific fine-tuning strategy, which our GeoMan method embodies, leading to more robust and reliable results.

Fine-Tuning Video ControlNet vs. Fine-Tuning UNet. Further investigation into the finer details of our approach reveals



Figure S13. Comparison with the existing depth estimation models. GeoMan produces the state-of-the-art results in both temporal consistency and fidelity.

a compelling insight into the critical components involved in fine-tuning. As illustrated in Fig. S17, we demonstrate that fine-tuning solely the Video ControlNet component is not sufficient to effectively adapt image-to-video diffusion models to the geometry estimation method. In contrast, our approach of fine-tuning the UNet component proves far more effective, facilitating a seamless transition from image-based generation to accurate video geometry estimation.

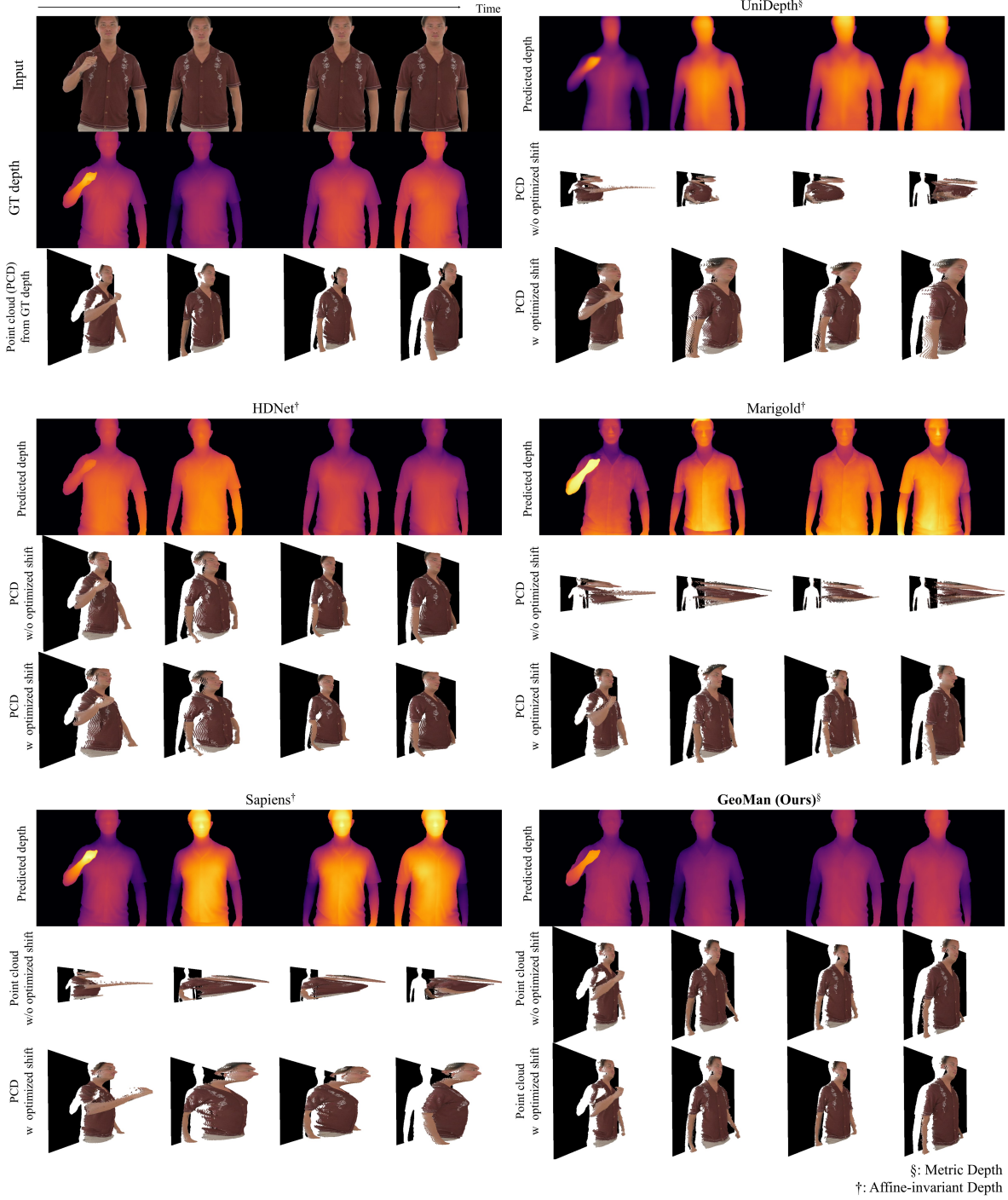


Figure S14. Comparison with the existing depth estimation models. GeoMan produces the state-of-the-art results in both temporal consistency and fidelity.

I2G vs. V2G. We present a detailed comparison between the per-frame estimations of the image-to-geometry (I2G) and the full GeoMan pipeline in Tab. S8(b). While I2G and GeoMan (I2G+V2G) exhibits similar accuracy, GeoMan outperforms I2G in temporal consistency. GeoMan pipeline excels in maintaining stability and coherence across frames, thereby ensuring smoother, more realistic video sequences. This superior temporal consistency is essential for high-quality video generation

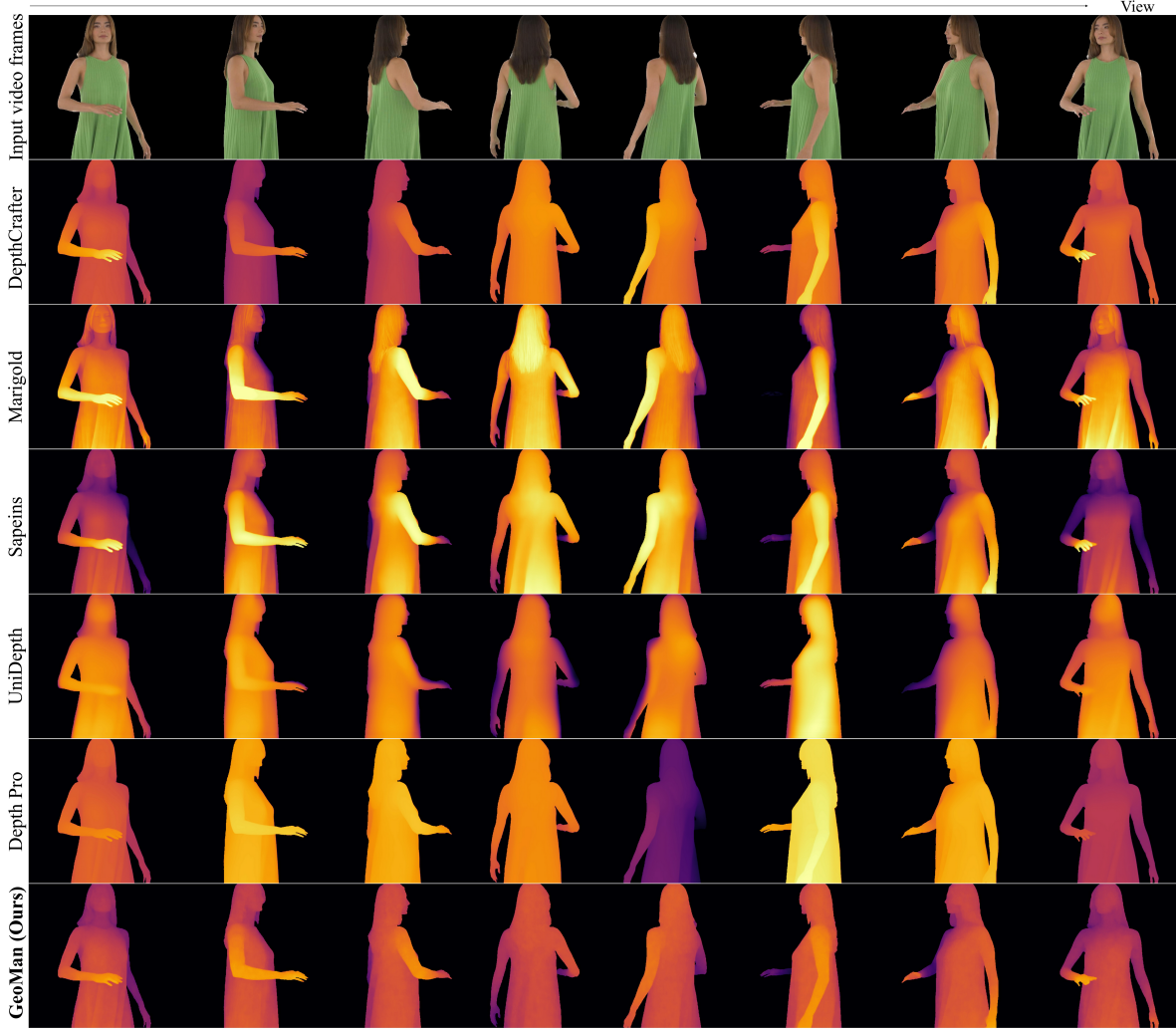


Figure S15. Comparison with the existing depth estimation models. GeoMan produces the state-of-the-art results in both temporal consistency and fidelity.

and demonstrates the power of GeoMan in addressing the challenges posed by dynamic visual content.

Multimodality of I2G. I2G faces challenges in multimodal modeling, as shown in Tab. S8(c), requiring modifications to input and output layers, which limits performance. While the V2G framework, involving similar tasks in image-to-video translation, benefits from fine-tuning a single model, enhancing efficiency and performance, I2G’s task divergence demands separate training for each modality.

Training Data Sources for V2G. In Tab. S8(d), we evaluate the impact of different training datasets on V2G. Training only on rotating videos generated from static 3D scans introduces artifacts caused by motion bias. On the other hand, using only low-resolution 4D data results in a lack of fine details, limiting the quality of predictions. By combining both datasets, we achieve the best results, with improved visual quality and enhanced temporal consistency.

Effectiveness of Human Area Crop. As demonstrated in Tab. S8(e), the use of human area cropping ensures that the model effectively targets relevant regions, thereby optimizing computational efficiency and accuracy. The positive impact of human area cropping confirms that focusing on key areas within the video frames is important, ensuring that unnecessary background noise does not interfere with the core task of human geometry estimation.

First-Frame Dependency. Replacing I2G predictions with ground truth improves performance as shown in Tab. 4 in the paper. Degrading the first frame by reducing its resolution by 4 times resulted in only a slight increase in error (Tab. S8(f), indicating the robustness of our model. The degraded version still outperforms other baselines, including Sapiens.

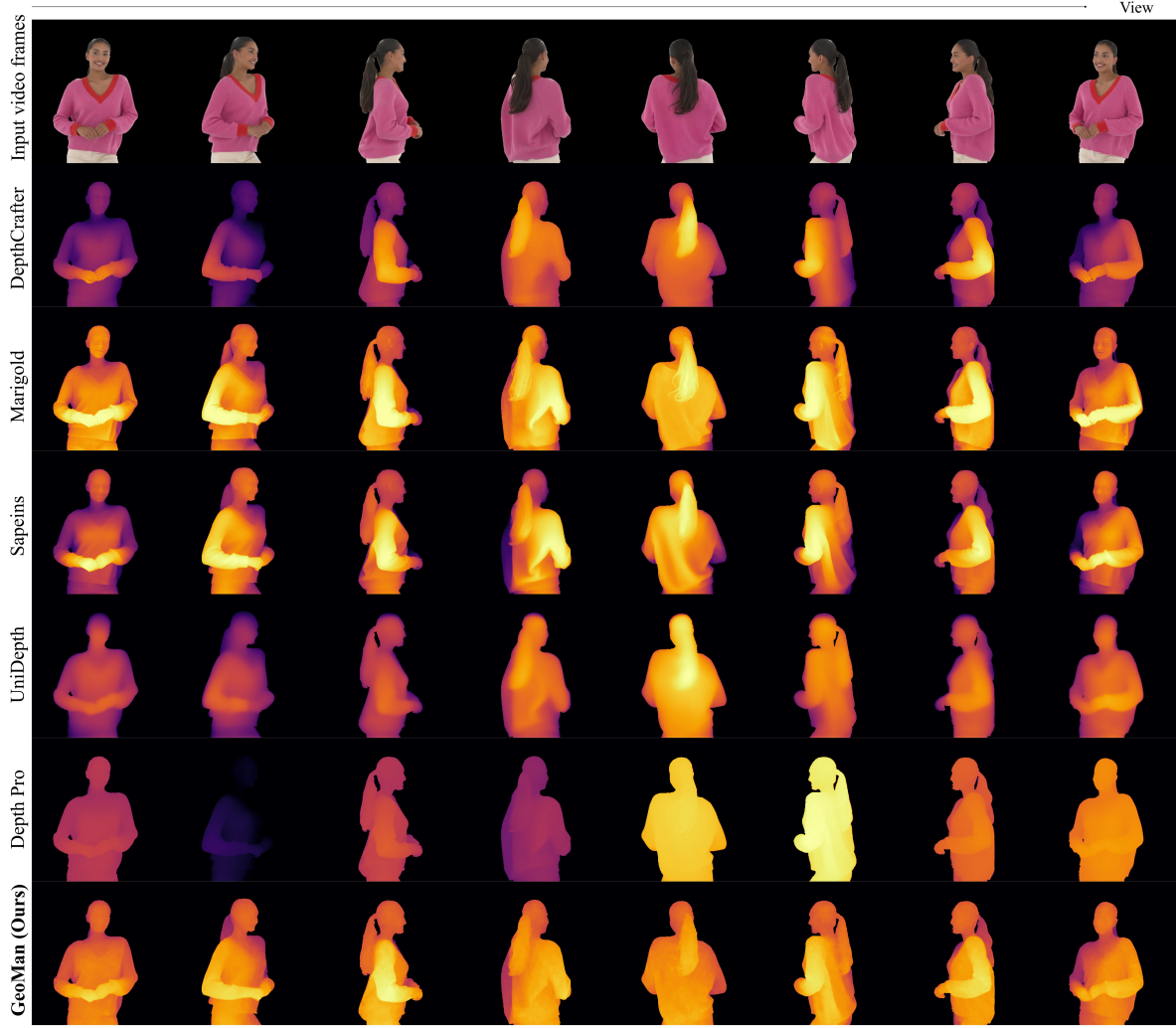


Figure S16. Comparison with the existing depth estimation models. GeoMan produces the state-of-the-art results in both temporal consistency and fidelity.

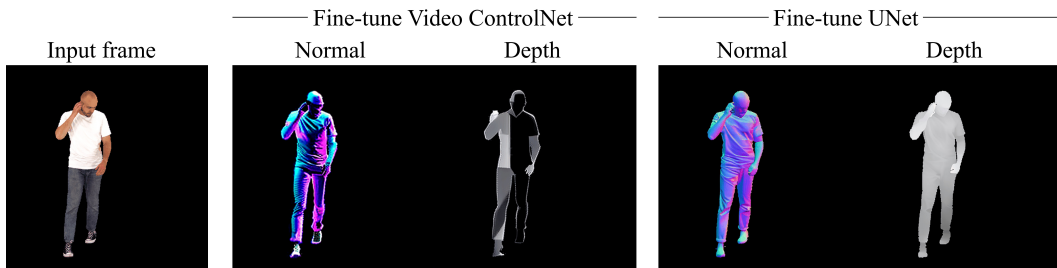


Figure S17. Fine-tuning the only Video ControlNet part is insufficient for reframing image-to-video diffusion models, whereas fine-tuning the UNet successfully transforms image-to-video generation into video geometry estimation.

Robustness & Generalizability. We’ve shown generalization to long videos, multiple persons, and drastic poses in the supp. video. Fig. S18 additionally highlights GeoMan’s robustness to diverse conditions, including occlusions, poor lighting, and atypical human types.

Efficiency Analysis. As shown in Tab. S9, GeoMan achieves competitive inference times compared to existing *diffusion*-

| | Normal | | | | | Depth | | | | | |
|---|--------------------|---------------|---------------|----------------------|--------------|------------------|-------------------------|--------------------------|-------------------------|----------------------|--------------|
| | Angular difference | | %within t° | Temporal consistency | | Optimizing shift | | Optimizing scale + shift | | Temporal consistency | |
| | Mean↓ | Median↓ | 11.25°↑ | OPW↓ | TC-Mean↓ | AbsRel↓ | $\delta < 1.05^\circ$ ↑ | AbsRel↓ | $\delta < 1.05^\circ$ ↑ | OPW↓ | TC-RMSE↓ |
| (a) Naïve extension vs GeoMan fine-tuning | | | | | | | | | | | |
| Naïve-5K-steps | 25.305 | 22.732 | 15.602 | 0.076 | 7.458 | 0.038 | 0.720 | 0.028 | 0.856 | 0.049 | 0.019 |
| Naïve-10K steps | 23.550 | 20.839 | 18.601 | 0.071 | 6.938 | 0.026 | 0.866 | 0.022 | 0.907 | 0.046 | 0.017 |
| Naïve-20K steps | 21.137 | 18.435 | 22.488 | 0.070 | 6.855 | 0.021 | 0.915 | 0.018 | 0.939 | 0.040 | 0.016 |
| Naïve-30K steps | 19.669 | 16.628 | 28.405 | 0.072 | 7.169 | 0.020 | 0.926 | 0.017 | 0.943 | 0.040 | 0.016 |
| Naïve-50K steps | 20.307 | 17.131 | 27.754 | 0.075 | 7.274 | 0.017 | 0.945 | 0.016 | 0.958 | 0.041 | 0.535 |
| GeoMan-5K steps | 17.499 | 13.541 | 40.340 | 0.069 | 6.781 | 0.014 | 0.964 | 0.013 | 0.970 | 0.036 | 0.014 |
| GeoMan-10K steps | 17.255 | 13.500 | 40.094 | 0.071 | 6.881 | 0.012 | 0.975 | 0.012 | 0.981 | 0.033 | 0.014 |
| GeoMan-20K steps | 16.548 | 12.719 | 43.483 | 0.066 | 6.502 | 0.012 | 0.977 | 0.011 | 0.984 | 0.032 | 0.014 |
| GeoMan-30K steps | 16.185 | 12.334 | 45.217 | 0.070 | 6.876 | 0.012 | 0.978 | 0.011 | 0.984 | 0.032 | 0.014 |
| GeoMan-50K steps | 16.105 | 12.144 | 45.995 | 0.067 | 6.599 | 0.012 | 0.975 | 0.011 | 0.983 | 0.033 | 0.015 |
| (b) I2G vs V2G | | | | | | | | | | | |
| I2G | 16.033 | 12.068 | 46.222 | 0.118 | 11.261 | 0.013 | 0.970 | 0.013 | 0.974 | 0.040 | 0.016 |
| I2G+V2G | 16.185 | 12.334 | 45.217 | 0.070 | 6.876 | 0.012 | 0.978 | 0.011 | 0.984 | 0.032 | 0.014 |
| (c) Multimodality of I2G | | | | | | | | | | | |
| Unimodal | 16.033 | 12.068 | 46.222 | 0.118 | 11.261 | 0.013 | 0.970 | 0.013 | 0.974 | 0.040 | 0.016 |
| Multimodal | 18.442 | 14.452 | 36.985 | 0.086 | 9.930 | 0.017 | 0.946 | 0.016 | 0.956 | 0.040 | 0.017 |
| (d) Training data source of V2G | | | | | | | | | | | |
| Only 3D data | 24.068 | 20.184 | 21.938 | 0.107 | 9.966 | 0.023 | 0.883 | 0.024 | 0.883 | 0.048 | 0.017 |
| Only 4D data | 16.387 | 12.441 | 44.787 | 0.062 | 6.198 | 0.013 | 0.967 | 0.012 | 0.980 | 0.035 | 0.015 |
| Combined | 16.185 | 12.334 | 45.217 | 0.070 | 6.876 | 0.012 | 0.978 | 0.011 | 0.984 | 0.032 | 0.014 |
| (e) Effectiveness of human area crop | | | | | | | | | | | |
| w/o Human area crop | 16.821 | 12.891 | 42.801 | 0.070 | 6.974 | 0.012 | 0.977 | 0.012 | 0.982 | 0.037 | 0.015 |
| w Human area crop | 16.185 | 12.334 | 45.217 | 0.070 | 6.876 | 0.012 | 0.978 | 0.011 | 0.984 | 0.032 | 0.014 |
| (f) Source of the First Frame for V2G | | | | | | | | | | | |
| 1/4 Downscaled I2G | 17.843 | 13.510 | 40.593 | 0.072 | 8.118 | 0.016 | 0.964 | 0.015 | 0.968 | 0.040 | 0.016 |
| I2G | 16.185 | 12.334 | 45.217 | 0.070 | 6.876 | 0.012 | 0.978 | 0.011 | 0.984 | 0.032 | 0.014 |

Table S8. Additional ablation studies. We validate the impact of various design choices.

| Method | GeoMan | Marigold | GeoWizard | IC-Light | ECON |
|----------|--------------|----------|------------|----------|----------|
| Time (s) | 10.57 | 8.44 | 23.34 | 7.854 | 134 |
| Method | Depthcrafter | Sapiens | Metric3Dv2 | UniDepth | DepthPro |
| Time (s) | 3.59 | 1.92 | 0.31 | 0.56 | 0.90 |

Table S9. Methods colored in red are diffusion-based, in violet is optimization-based, in blue are feed-forward.

based methods, though it is slower than some other baselines. However, Geoman has clear benefits: significantly improved temporal consistency, richer 3D detail, and enhanced human-specific understanding. While inference time increases with ensemble size or the number of diffusion steps, this trade-off is adjustable and can be tuned per application. We envision GeoMan as a practical tool for acquiring large-scale, real-world supervision, enabling its distillation into the next generation of faster, lightweight human geometric estimation models.

C. Limitations and Future Works

For in-the-wild applications, our method relies on matting techniques to separate the subject from the background, making its performance inherently dependent on matting accuracy. Additionally, metric depth reconstruction is constrained by the precision of 3D human pose estimation, particularly the accuracy of pelvis root depth estimation. Due to VRAM limitations, we trained our model at a maximum resolution of 512, fitting within 80GB of NVIDIA A100 GPUs with a batch size of 1. While our approach produces detailed and high-quality geometry, we plan to explore lightweight models or alternative training strategies to enable higher-resolution generation.

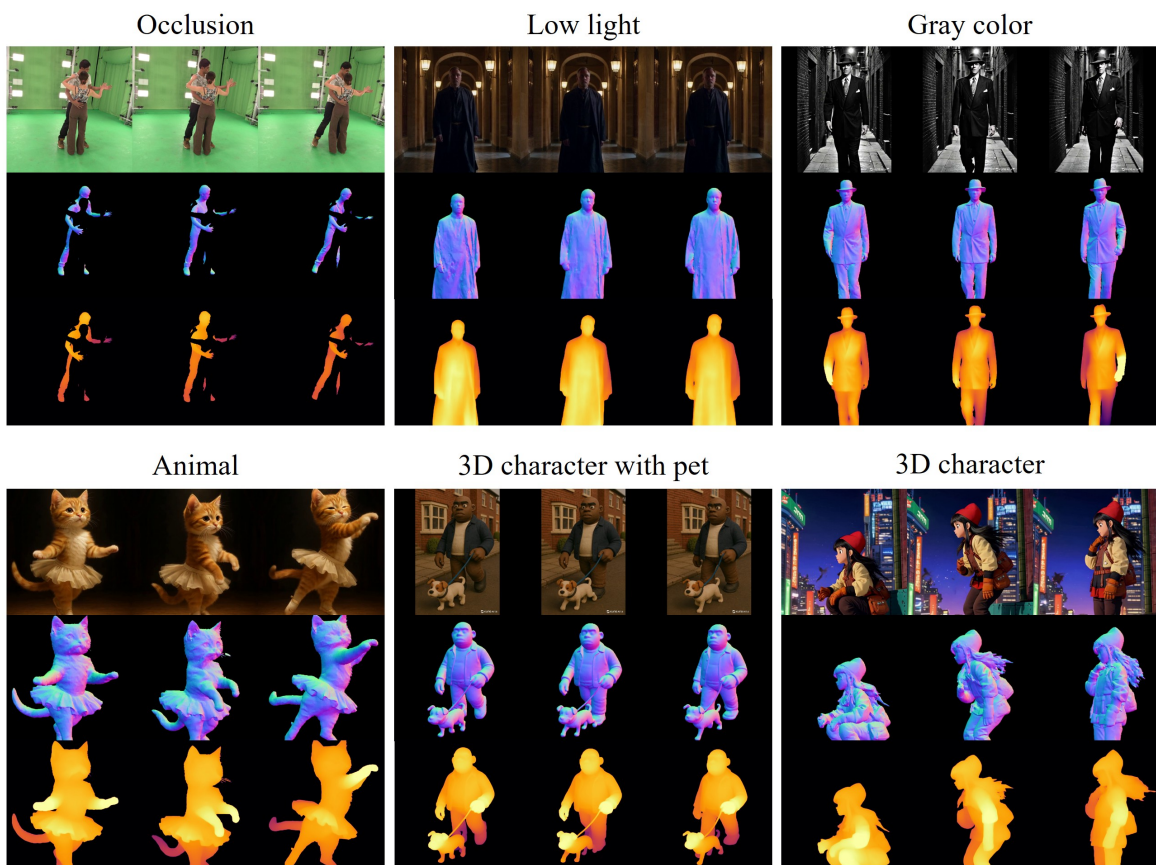


Figure S18. GeoMan demonstrates generalizability across diverse scenarios, including occlusions, low lighting, and atypical human types.